

**PATIENT STUDIES ON SHADING CORRECTION FOR
CONE-BEAM COMPUTED TOMOGRAPHY IMAGES**

A Thesis
Presented to
The Academic Faculty

by

Tiffany Tsui

In Partial Fulfillment
of the Requirements for the Degree
Master of Science in Medical Physics in the
School of Nuclear & Radiological Engineering & Medical Physics
The George W. Woodruff School

Georgia Institute of Technology
May 2015

COPYRIGHT© 2015 BY TIFFANY TSUI

**PATIENT STUDIES SHADING CORRECTION FOR CONE-BEAM
COMPUTED TOMOGRAPHY IMAGES**

Approved by:

Dr. Lei Zhu, Advisor

School of Mechanical Engineering, Medical Physics

Georgia Institute of Technology

Dr. Eric Elder

Department of Radiation Oncology

Emory University School of Medicine

Dr. Justin Roper

Department of Radiation Oncology

Emory University School of Medicine

Date Approved: December 17th, 2014

*I dedicate my work to
my parents, Wing Sing and Amy,
for their endless love and patience,
my beloved sisters and brother, Carolyn, Melanie, and Brandon,
who have been there for me through my ups and downs,
and all my friends,
who have encouraged and supported me.*

ACKNOWLEDGEMENTS

I would like to express my deepest gratitude to my advisor, Dr. Lei Zhu, for his excellent guidance, patience, and for providing me with the great resources and atmosphere for doing research. I would like to thank my committee members, Dr. Eric Elder and Dr. Justin Roper, for their advice and guidance throughout this research project and my graduate studies at the Georgia Institute of Technology.

I want to give my sincere thanks to my fellow labmates, Michael Petrongolo and Tonghe Wang, for helping me from time to time throughout this research project.

I would also like to thank Dr. Tim Fox and Mr. Antony Waller from Varian Medical Systems for their advice regarding how to use Varian Velocity software. I would like to thank Dr. Eduard Schrebmann from Emory University and Dr. Yi Gao from Stony Brook University for their advice and help regarding image registration.

Special thanks to Dr. Jikun Wei from Cancer Treatment Centers of America (CTCA) for his support throughout this research project.

Last but not least, I want to thank all my family and friends for their love and support throughout my education.

TABLE OF CONTENTS

	Page
ACKNOWLEDGEMENTS	iv
LIST OF TABLES	vi
LIST OF FIGURES	vii
LIST OF ABBREVIATIONS	viii
LIST OF SYMBOLS	ix
SUMMARY	xi
CHAPTER 1 - INTRODUCTION	1
CHAPTER 2 - BACKGROUND	3
2.1 The role of CBCT and pCT in IGRT	3
2.2 Hounsfield unit and linear attenuation coefficient	6
2.3 CT reconstruction	7
2.3.1 Flat fields and line integral	7
2.3.2 Image reconstruction	8
2.3 Rigid and deformable registration	9
2.4 Image artifacts	10
2.5 Paired t-test	11
2.6 Varian's method for CBCT shading correction	13
CHAPTER 3 - METHODS	14
3.1 Method for image correction	14
3.2 Method for statistical evaluation	18
3.2.1 Mean CT number, SNU values, and image contrast	18
where C error is the error of image contrast, CpCT is the contrast value of the	
ground true, and Ccorrected CBCT is the contrast value of the shading corrected	
CBCT.	21
3.2.2 Paired t-test	21
CHAPTER 4 - RESULTS	25
4.1 Qualitative results	25
4.1.1 Axial view images	25
4.1.2 Coronal and sagittal view images	28
4.2 Quantitative results	31
4.2.1 Axial view images	32
4.2.2 Coronal view images	34
4.2.3 Sagittal view images	36
CHAPTER 5 - DISCUSSION	38
CHAPTER 6 - CONCLUSION	42
APPENDIX A - RAW DATA	43
APPENDIX B - ERRORS IN CT NUMBERS, SNU, AND CONTRAST VALUES FOR	
ALL PATIENT DATA	54
REFERENCES	63

LIST OF TABLES

	Page
Table 1: Summary of average errors in CBCT corrected by Varian and proposed methods	31
Table 2: Average errors in CT numbers, SNU, and contrast values for images in axial view	32
Table 3: Values for paired t-test calculations for axial view	34
Table 4: Average errors in CT numbers, SNU, and contrast values for images in coronal view	35
Table 5: Values for paired t-test calculations for coronal view	35
Table 6: Average errors in CT numbers, SNU, and contrast values for images in sagittal view	36
Table 7: Values for paired t-test calculations for sagittal view	37
Table 8: Image details of the 20 sets of patient data	43
Table 9: Raw and mean CT values of axial images for 20 patient data sets	45
Table 10: Raw and mean CT values of coronal images for 20 patient data sets.	48
Table 11: Raw and mean CT values of sagittal images for 20 patient data sets	51
Table 12: RMSE values of axial images	54
Table 13: SNU values and errors of axial images	55
Table 14: Image contrast values and errors of axial images	56
Table 15: RMSE values of coronal images	57
Table 16: SNU values and errors of coronal images	58
Table 17: Image contrast values and errors of coronal images	59
Table 18: RMSE values of sagittal images	60
Table 19: SNU values and errors of sagittal images	61
Table 20: Image contrast values and errors of sagittal images	62

LIST OF FIGURES

	Page
Figure 1: Acquisition geometry comparison.....	5
Figure 2: Output of CT.	8
Figure 3: t-distribution curve	12
Figure 4: Workflow of image preprocessing.	15
Figure 5: Workflow of shading correction for CBCT image.....	16
Figure 6: Four selected uniform soft-tissue ROIs in axial images.....	19
Figure 7: First example of successful shading corrected axial CBCT images (Patient A) amongst 20 sets of total sample size.	26
Figure 8: Second example of successful shading corrected axial CBCT images (Patient B) amongst 20 sets of total sample size.	27
Figure 9: First example of challenging axial CBCT images (Patient H) for shading correction.	27
Figure 10: Second example of challenging axial CBCT images (Patient L) for shading correction.	28
Figure 11: First example of successful shading corrected CBCT images (Patient A) in coronal and sagittal views.	29
Figure 12: Second example of successful shading corrected CBCT images (Patient B) in coronal and sagittal views.	29
Figure 13: First example of challenging images (patient H) in coronal and sagittal views for shading correction.	30
Figure 14: Second example of challenging images (patient L) in coronal and sagittal views for shading correction.	30
Figure 15: Unsuccessful image registration for thorax images.	41

LIST OF ABBREVIATIONS

CBCT	Cone Beam Computed Tomography
CNR	Contrast-to-noise ratio
CT	Computed Tomography
CTCA	Cancer Treatment Centers of America
FBP	Filtered backprojection
FDK	Feldkamp, Davis, and Kress
HU	Hounsfield unit
IGRT	Image-guided radiation therapy
kV	Kilovoltage
MDCT	Multi-detector computed tomography
MRI	Magnetic resonance imaging
MV	Megavoltage
OBI	On-board imager
pCT	Planning Computed Tomography
PET	Position emission tomography
PWLS	Penalized weighted least square
RMSE	Root mean square error
ROI	Region of interest
SKS	Scatter Kernel Superposition
SNR	Signal to noise ratio
SNU	Spatial non-uniformity
VMS	Varian Medical Systems
VOI	Volume of interest

LIST OF SYMBOLS

A	Atomic mass
Z	Atomic number
N_{Av}	Avogadro's number
α	$(1 - \alpha)$ is the confidence level in t-test
ν	Degree of freedom
ρ	Density of tissue in a voxel
δ	Difference between the mean values of two populations
i	Index of ROI
C	Image contrast value
μ	Linear attenuation coefficient
μ_{comp}	Linear attenuation coefficient for Compton scattering
\overline{HU}_{max}	Maximum HU value in the selected ROIs
\overline{HU}_{min}	Minimum HU value in the selected ROIs
μ_1	Mean values of first population (Varian correction method)
μ_2	Mean values of second population (Proposed correction method)
x_b	Mean value in background area of the CT image
x_i	Mean value inside ROI of the CT image
x_i'	Mean value inside ROI of the reference image
n	Number of samples
\hat{u}_1	Sample mean values of first population (Varian correction method)
\hat{u}_2	Sample mean values of second population (Proposed correction method)
s_1	Standard deviation of first population (Varian correction method)
s_2	Standard deviation of second population (Proposed correction method)
$t_{\alpha,\nu}$	t value at the confidence level of $(1 - \alpha)$ and with ν degrees of freedom

t	Test statistic T
z	Test statistic Z
N	Total number of ROIs
σ_1^2	Variance of first population (Varian correction method)
σ_2^2	Variance of second population (Proposed correction method)

SUMMARY

The work performed and presented in this thesis explores the efficacy of using planning Computed Tomography (CT) images as prior knowledge to improve quantitative cone-beam CT (CBCT) image quality in radiation therapy. CBCT is a significant component in the treatment planning process of image-guided radiation therapy (IGRT). Current CBCT images have various shading artifacts such as scatter, noise, and non-uniformity that create challenges in accurately identifying tissue abnormalities and reduce their usefulness for clinical applications. This thesis proposes a method to enhance the CBCT image quality when using commercial image correction methods (i.e. images corrected by a Varian algorithm). The results show that scattering and image non-uniformity are greatly reduced by the proposed method. Therefore, the proposed method achieves better image correction results than does the Varian correction algorithm.

Since all patients who receive radiation treatment routinely undergo a multiple detector array CT (MDCT) scan as part of the diagnostic procedure, the high quality MDCT serves as the “free” planning CT (pCT). To improve the CBCT images that are taken during radiation treatment, the CBCT is first spatially registered with the pCT via rigid and deformable registration using Velocity software. Primary projections in the CBCT scan are estimated via forward projections of the registered MDCT image. The low frequency errors in the projections, which are a major cause of shading artifacts in CBCT images after reconstruction, are estimated by filtering the difference between the

original line integral and the estimated scatter projections. The corrected CBCT image is then reconstructed from the projections using the Feldkamp, Davis, and Kress (FDK) algorithm. With the planning MDCT treated as ground truth, the CBCT image corrected by the proposed method is compared against the corrected image using the Varian Medical Systems (VMS) algorithm, a commonly used commercial shading correction method. The results are presented in the axial, coronal, and sagittal views, and are evaluated by comparing the mean number of error for three image quality evaluation factors - CT number, spatial non-uniformity (SNU) value, and image contrast value. A paired t-test is performed on the results to prove the consistency and reliability of the proposed method of shading correction.

The proposed method is evaluated on 20 sets of thorax and pelvis cancer patient data from Cancer Treatment Centers of America (CTCA). CT numbers, measured in Hounsfield units (HU), for four uniformly selected regions of interests (ROIs) are found in each set of images. The mean errors in CT number, SNU, and contrast value for the Varian corrected image and the image corrected by the proposed method are 53 HU and 41 HU, 7.3% and 3.0%, and 37 HU and 34 HU respectively. The results show that as compared to the Varian correction algorithm the proposed method delivers a CBCT image quality with better spatial uniformity and fewer CT number errors at the 95% confidence level, and with statistically insignificant but comparable change in image contrast.

Promising results have previously been obtained using similar methods on CBCT tabletop phantoms and a limited amount of prostate patient data sets [1]. As an extension of previous work performed by Niu et al [2], the proposed method is modified and evaluated using 20 sets of thorax and pelvis cancer patient data, which includes both male and female patients. Statistical analysis is performed and confirms that the proposed method can be employed within the current CBCT shading correction algorithm used by VMS to greatly enhance CBCT image quality.

CHAPTER 1 - INTRODUCTION

The use of computed tomography (CT) is a key tool in radiotherapy. Accurate localization of the entire tumor volume and surrounding normal tissue is required to administer the prescribed dose for the treatment of malignant diseases. Currently, quantitative CBCT imaging is commonly used in IGRT for three-dimensional on-board x-ray imaging and increases the accuracy of identifying various tissues and bone structures.

Radiation therapy typically involves three components: simulation, treatment planning, and radiation delivery. Simulations are performed to determine the treatment position that a cancer patient will use daily. During simulation, high quality diagnostic MDCT images are acquired as the pCT a few days prior to commencing treatment. The pCT images are then used to create a treatment plan, which is customized to each individual cancer patient. Before IGRT was used in clinical practice, patients were only imaged periodically before and during treatment. Nowadays, CBCT images are taken every day before delivering each fraction of radiation to help ensure that the patient's position in the treatment room matches that of the pCT images. This greatly increases the accuracy of patient setup and allows precise comparison of the image obtained immediately before the treatment with the reference image used for planning.

Clear and high quality CT images allow physicians to precisely delineate the gross tumor volume (GTV), planning treatment volume (PTV), and normal surrounding

organs at risk (OAR) in order to deliver the highest possible dose to the tumor volume and the lowest possible dose to the surrounding healthy tissue. The results presented in this thesis show that the CBCT image corrections obtained with a current industrial algorithm can be greatly improved by using MDCT as prior knowledge via a combination of image registration techniques, forward projection algorithms, and reconstruction algorithms, as shown in the proposed correction method.

CHAPTER 2 - BACKGROUND

On-board x-ray imaging has evolved from two to three dimensions, and x-ray CT has become an important tool in medical imaging since its introduction in 1970s. CT provides detailed, three-dimensional cross-sectional images within which a physician can distinguish various tissues, and hence it is commonly used for diagnosing tumors in the chest, abdomen, and pelvis (for example, lung, pancreatic, liver, and prostate cancer). Therefore, high CT image quality is vital in radiation therapy. This section of the thesis provides background information regarding the role of CBCT and pCT in IGRT, how forward projection, image reconstruction, and scatter estimation help with image correction, how image registration relates to the geometry differences between pCT and CBCT, and how VMS corrects shading artifacts in CBCT images.

2.1 The role of CBCT and pCT in IGRT

In IGRT using an on-board imager (OBI), the patient is positioned prior to treatment by aligning planar images taken immediately before treatment with pCT images taken during simulation. Alignment is based upon internal anatomy with high contrast materials, for example bones and internal markers. Aligning treatment images with planning images helps ensure accurate dose delivery, because a patient's internal organs (e.g. prostate position due to bladder volume) or daily setup may not have the exact same relative positions as during simulation. OBI has several choices for imaging modalities, including two-dimensional radiographic imaging and three-dimensional kV

CBCT imaging. The latter is performed by rotating the gantry, which contains a fixed x-ray source and detector, around the patient and then reconstructing three-dimensional tomographic images from two-dimensional projection data. kV CBCT is frequently used due to its ability to generate volume images of patients.

Conventional CT and CBCT acquire three-dimensional representations of objects differently. A conventional helical CT uses fan-shaped or spiral x-ray beams to acquire image slices. The slices are then stacked to form a three-dimensional view. On the other hand, CBCT uses a divergent pyramid-shaped ionizing radiation source that is directed through the middle of the volume of interest (VOI) onto a detector behind the object. When the x-ray source and the detector rotate around the object, planar projection images are acquired in a complete arc. The two-dimensional projection images are then reconstructed into three-dimensional axial tomographic images via a reconstruction algorithm. The comparison of conventional CT acquisition geometry to CBCT acquisition geometry is shown in Figure 1. With cone-beam geometry, x-ray beams are projected to form multiple projections, which are later reconstructed into orthogonal planar images. In the conventional CT fan-beam geometry, axial slice image data are taken and stacked to generate orthogonal images [3].

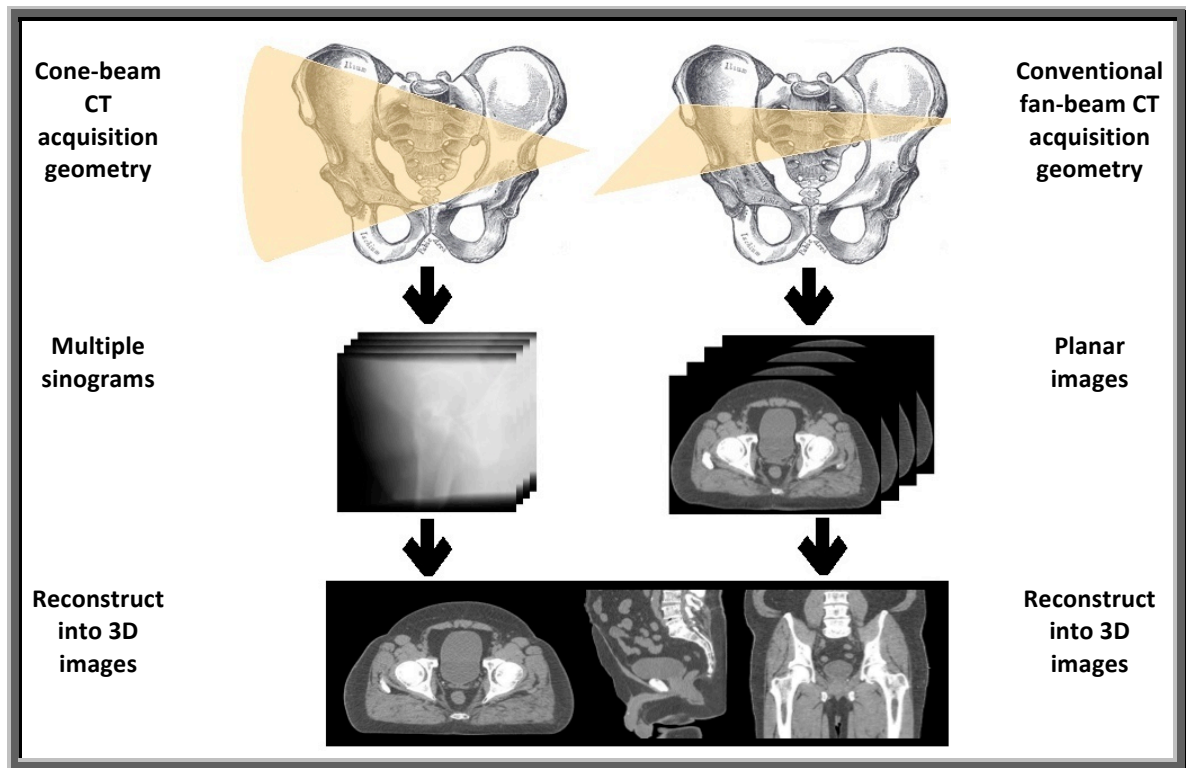


**Figure 1: Acquisition geometry comparison.
Cone beam CT (left) and conventional CT (right)**

MDCT is a form of CT technology for diagnostic imaging and is often used as pCT to plan a patient's treatment. MDCT can acquire higher resolution CT images in a shorter period of time or with larger patient coverage because it has a two-dimensional array of detector elements that replaces the linear array of detector elements used in other conventional CT scanners. Compared to single slice CT system, MDCT can acquire faster scanners and thinner slices.

2.2 Hounsfield unit and linear attenuation coefficient

Unlike those of other imaging modalities, such as PET or MRI, CT images depict the x-ray attenuation properties of materials, which are closely related to electron density through Compton scattering, i.e. the primary mode of attenuation during diagnostic imaging. The linear attenuation coefficient of Compton scattering is proportional to the tissue mass density in a voxel, the atomic number, and atomic mass as shown in Eqn (1).

$$\mu_{comp} \propto \rho N_{Av} \frac{Z}{A} \quad \text{Eqn (1)}$$

where μ_{comp} is the Compton scattering linear attenuation coefficient, ρ is the mass density of tissue, N_{Av} is the Avogadro's number (6.023×10^{23}), A is the atomic mass, and Z is the atomic number. Pixels within CT images represent linear attenuation coefficient (μ) values in terms of the Hounsfield unit (HU), and are displayed in gray scale. The HU is defined as in Eqn (2) [4].

$$HU_{(x,y,z)} = 1000 \times \frac{(\mu_{(x,y,z)}) - \mu_w}{\mu_w} \quad \text{Eqn (2)}$$

where $\mu_{(x,y,z)}$ is the average linear attenuation coefficient of a voxel of tissue with the location (x, y, z) , and μ_w is the linear attenuation coefficient of water at the same photon energy.

2.3 CT reconstruction

The relationship amongst flat field projections, line integrals, forward projections, and image reconstruction will be discussed in this section.

2.3.1 Flat fields and line integral

The raw data used for any image reconstruction and correction algorithms includes the air scan, also known as the flat field projection, and the measured projection data. Flat field projections characterize the influence of bow tie filters and variation in individual detector responses (e.g. difference in amplifier) during routine calibration of the CT scanner. Flat field projections serve as calibration scans, which helps to detect any missing or dead pixels and to normalize the measured projection data.

Since x-ray attenuates exponentially upon interactions, as described in Eqn (3), the measured projection data undergoes logarithmic transformation and normalization. The projection measurements, also known as the line integral, are derived from Eqn (3) and shown in Eqn (4).

$$I = I_0 e^{-\mu_L x} \quad \text{Eqn (3)}$$

$$P = \ln \left(\frac{I_0}{I} \right) \quad \text{Eqn (4)}$$

where I is the x-ray intensity after attenuation, I_0 is the x-ray intensity before attenuation, μ_L is the linear attenuation coefficient, and x is the attenuation distance.

The projection measurement is the logarithm that converts the exponential nature of x-ray absorption into a line of integrals and is illustrated in Figure 2. I_r is the output of a CT scanner without a patient present. Hence I_r is the flat field projection. I_j is the measured signal after the beam passes through a patient's anatomy as shown in Figure 2. As such, I_j is the result of beam attenuation by a number of different tissues lying along the beam path, each having its own linear attenuation coefficient.

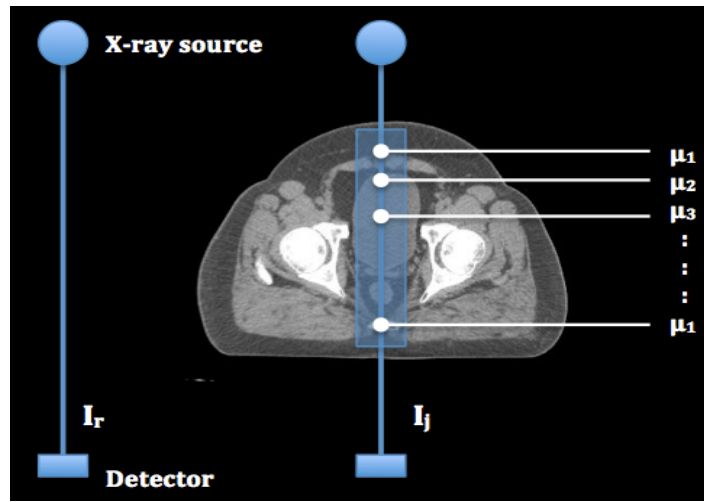


Figure 2: Output of CT.

The reference detector (I_r) is positioned outside the patient anatomy to measure flat field. I_j measures the linear attenuation coefficient values (μ) along the path ray through the patient anatomy [4].

2.3.2 Image reconstruction

Using CBCT with medical linear accelerators is beneficial for IGRT because it can provide volumetric imaging and allow radiographic monitoring throughout the

patient's treatment process. CBCT can acquire many cross-sectional images, i.e. projections 360 degrees over the entire VOI. Some projections (at 0, 90, 180, and 270 degrees) can be recognized as the coronal and sagittal views of a VOI. However, most projections, which contain anatomic information, are difficult for people to visualize without reconstructing these projections into axial slices. Individual axial slices of objects in a conventional fan-beam CT can be sequentially reconstructed using filtered back projection (FBP). However, as CBCT reconstruction uses two-dimensional projections rather than projections of axial slices, alternative methods to FBP are needed. Image reconstruction from CBCT projections collected along a single circular source trajectory can be achieved using the FDK algorithm with convolution-backprojection method. FDK, which converts the projection data into CT images, takes the cone angle into account and is commonly used for cone-beam reconstruction due to ease of implementation. However, resolution degradation in the end slices of transverse planes is unavoidable and requires further research and study for improvement.

2.3 Rigid and deformable registration

Image registration aligns two images, which are of the same object but acquired at different times or using different modalities, within the same coordinate system. It plays an important role in IGRT as image registration links the images of a patient's anatomy taken during the simulation and planning process to the images taken during the treatment process. There are several types of image registration, with the two main groups being rigid and deformable registration.

Rigid registration has a total of six degrees of freedom, i.e. three rotational variables and three translational variables. Thus, it allows the secondary image to rotate and translate to match the primary image. On the other hand, deformable registration has a huge number of degrees of freedom and allows for better results with higher accuracy compared to rigid registration. The matrix for deformable registration is complicated, and it generally requires four major components, which are an interpolator, a similarity metric (e.g. Mutual information), a transformation, and an optimizer.

2.4 Image artifacts

One reason to favor CBCT exams over other conventional CT exams is that the total radiation dose from CBCT is generally lower. Despite the common use of CBCT, the technique still has its limitations and is susceptible to image artifacts. Examples of artifacts observed in CBCT images include streaking artifacts, motion artifact, beam hardening, and noise.

Streaking artifacts can be caused by multiple factors, including photon starvation, undersampling, motion, and beam hardening. They are usually found around high contrast materials, e.g. bony structures and metals, because most x-rays cannot travel through those materials and photon inelastic scattering (known as Compton scattering) may occur. The photon starvation artifact is frequently found when the slice thickness is thin, because it causes additional noise and streaking along the paths of high x-ray

attenuation when too few photons reach the detector. Undersampling in the cone angle dimension creates deficits in the acquired data and is a common cause of cone beam artifacts.

Motion artifacts are one of the most common factors that hinder the image quality of CBCT. Since it takes a while to acquire data, patients have time to move while being imaged, which introduces motion artifacts that appeared as blurring or streaking in the image.

Non-uniform shading is apparent in many CBCT images. The effect of cupping artifacts and dark bands or streaks in the middle of highly attenuating objects is due to beam hardening. Beam hardening occurs when the mean energy of an x-ray beam, which is composed of a range of photon energies, increases or becomes “harder”. Beam hardening results from lower-energy photons being more easily attenuated by tissues than higher-energy photons. Since a beam that passes through the center of a patient or an imaged object typically travels through thicker amounts of material than a beam that passes through the periphery, cupping artifacts occur.

2.5 Paired t-test

The statistical significance of the difference between the two sets of corrected images can be analyzed using paired t-tests. A group of corrected images (i.e. images corrected by Varian method or the proposed method) can be modeled as a normal

population with the mean μ and the variance σ^2 . The normal population has a t-distribution, as shown in Figure 3. The t value with a defined degree of freedom (ν) and confidence level ($1 - \alpha$) is found in any published t-distribution statistics tables. ν is defined as the number of values in a statistic calculation that are free to vary, as shown in Eqn (5).

$$\nu = n - 1 \quad \text{Eqn (5)}$$

α is calculated as the threshold value that one measures against the t-value from the distribution table. The confidence level is related to α by Eqn (6).

$$\text{confidence level} = 1 - \alpha \quad \text{Eqn (6)}$$

when variances in the two populations are known, the t-value follows Eqn (7).

$$t = \frac{\hat{u}_1 - \hat{u}_2 - \delta}{\sqrt{\frac{\sigma_1^2}{n_1} + \frac{\sigma_2^2}{n_2}}} \quad \text{Eqn (7)}$$

where $\hat{u}_1 - \hat{u}_2$ is the difference in sample means and δ is the difference in population mean values. On the other hand, when variances in the two populations are unknown, the t-value follows a slightly different equation, which will be explained later in section 3.2.2 [5].

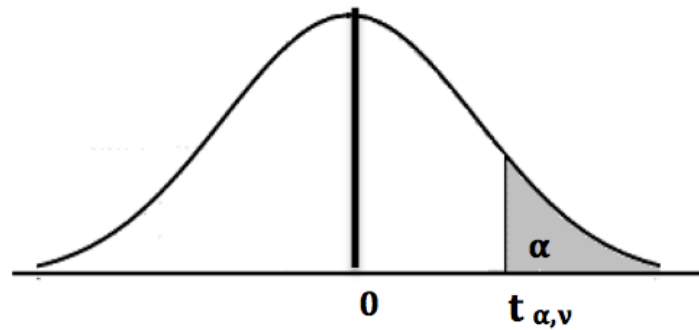


Figure 3: t-distribution curve

2.6 Varian's method for CBCT shading correction

Varian Medical Systems (VMS) employs an asymmetric kernels technique [6] to correct scatter artifacts in CBCT images. The scatter kernel superposition (SKS) method is a well-known correction technique that involves the scatter point-spread functions generated by pencil beam and deriving the kernels that deconvolute projection. The accuracy of the SKS algorithm is improved by replacing the traditionally used symmetric kernels with the asymmetrical kernels. The asymmetric kernel substantially improves scatter estimates and hence effectively corrects shading artifacts including beam hardening and lag.

CHAPTER 3 - METHODS

3.1 Method for image correction

The original CBCT line integral projections and CT images are first preprocessed. The file format of the planning MDCT images and the Varian corrected CBCT images are converted from DICOM to .raw files with the corresponding metadata (.mhd) using C code. The file format of the line integral projections is converted from .xim to .raw using a MATLAB code. The .raw file format can be viewed and manipulated using Image J. The preprocessing stage also includes changing the CT intensity units from HU to linear attenuation coefficient, and segmenting out the benches in the CT images to increase the quality of image registration. The last step can be neglected if the CBCT projection field does not cover the metal frame, or if the ROI of image registration can be manually adjusted in the registration software. The stage of image preprocessing is illustrated in Figure 4.

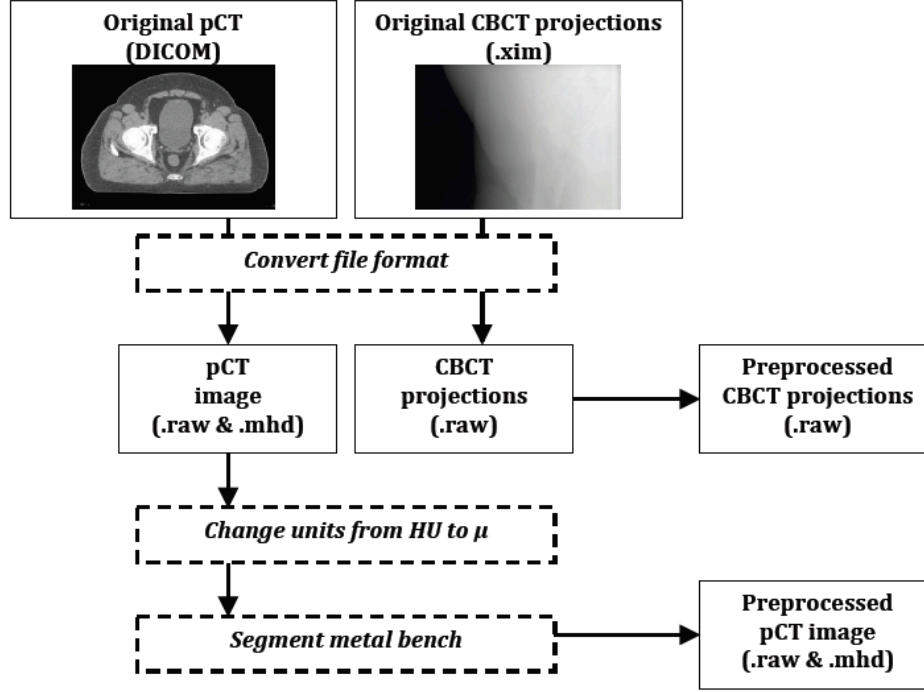


Figure 4: Workflow of image preprocessing.

The overall workflow of improving the image quality of CBCT using planning MDCT as a prior knowledge is shown in Figure 5. As outlined in the figure, the proposed method uses the high quality MDCT image as “free” prior information to improve the quality of CBCT images that are corrected by current industrial methods, e.g. Varian algorithm. Hence, rigid and deformable registrations are performed on the Varian corrected CBCT images and MDCT images for each patient data sets using the Velocity software. The Varian corrected CBCT is used as the fixed image (i.e. primary image) and the MDCT is used as the moving image (i.e. secondary image). The ROI used for image registration is manually adjusted to eliminate the metal bench or any other high-contrast materials in the background that may hinder the effect of image registration. Registration between the primary and secondary images is performed under the rigid and deformable multi pass mode.

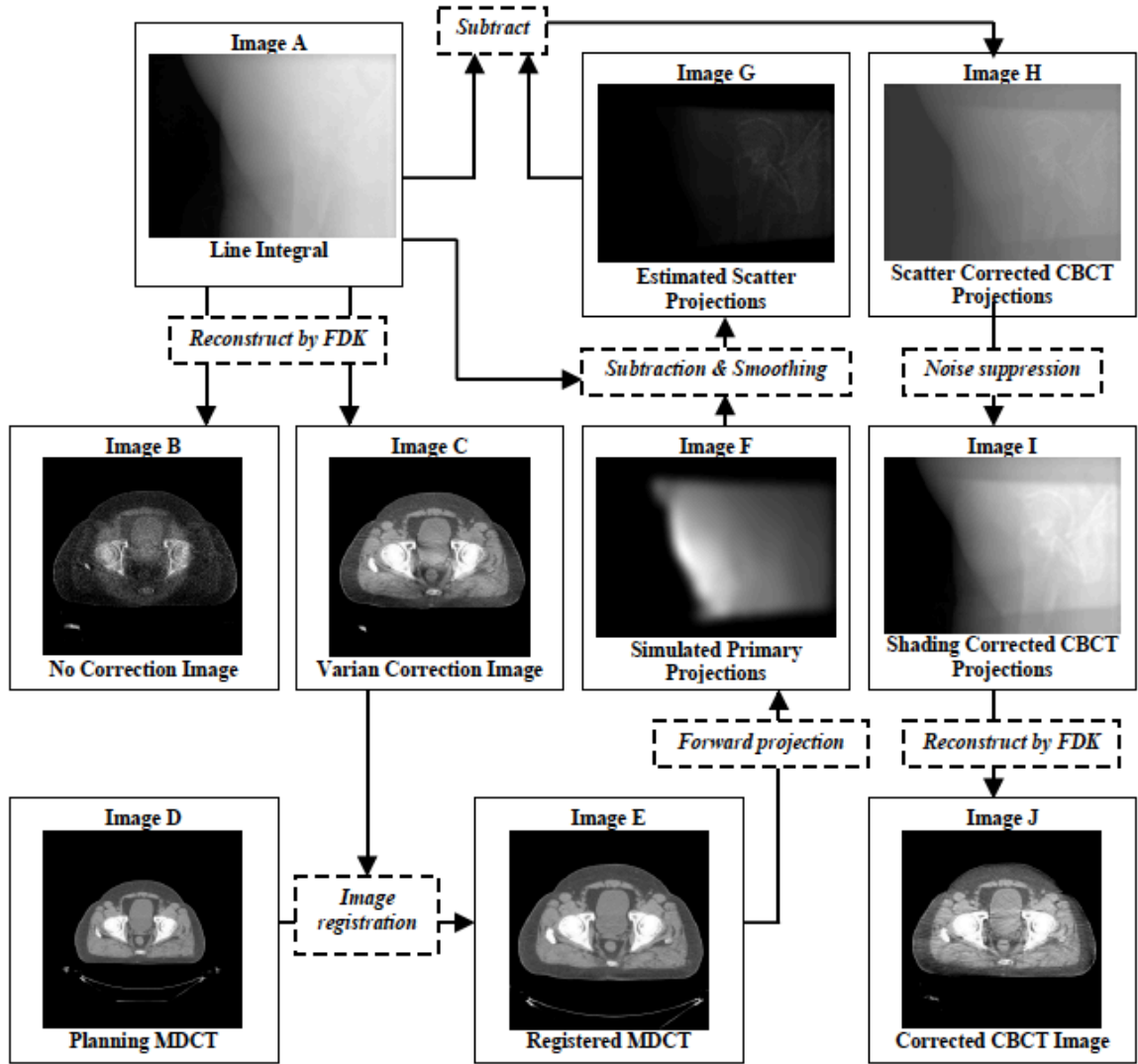


Figure 5: Workflow of shading correction for CBCT image

The primary projections in the CBCT scan are simulated via forward projection of the registered MDCT. The estimated scatters in projections, which are the low frequency errors in the projections that cause most of the scatter artifacts in CBCT images, can be estimated with great confidence by finding the difference between the simulated primary projections and the line integral projections. The performance of the proposed shading

correction method is greatly enhanced when the estimated scatter is smoothed. During the smoothing of the estimated scatter in projections, the boundary discrepancy between the original line integral projections and the estimated scatter projections is suppressed by a 2D median filter, which has the dimensions of 51 by 51 pixels on the detector. The high frequency primary differences between the two projections are further suppressed using a low-pass 2D Gaussian filter, which can effectively reduce high frequency errors without hindering the low frequency scatter signals. The low-pass 2D Gaussian filter is set to have the parameter of 41 by 41 pixels and a standard deviation of 21 pixels. The scatter corrected CBCT projection is then generated by subtracting the smoothed scatter errors from the original line integral projection. To save computation time, the initial voxel dimensions are downsampled by a factor of 4. Sampling is restored to full resolution after the estimated scatter projections are obtained. On a 2.66 GHz CPU workstation, the forward projection step to obtain the simulated primary projections and the smoothing step to obtain the estimated scatter projections each take about 40 seconds per projection.

The PWLS algorithm [7] is applied on the scatter corrected CBCT projections to suppress image noise. Finally, the shading corrected CBCT projections are reconstructed into shading corrected CBCT images using the FDK algorithm. The corrected projections are reconstructed to 81 CT image slices to match the number of Varian corrected CBCT image slices for a fair and clear image comparison. Each projection takes about 40 seconds to complete. Thus, the image reconstruction of 81 CT slices from 654 to 656 projections takes approximately 5.6 hours to complete on a 2.66 GHz CPU workstation.

The relationship between the line integrals, simulated primary projections, estimated scatter projections, and scatter corrected projections are shown in Figure 5.

The quality of CBCT images corrected by the Varian method and the proposed method are qualitatively compared against the CBCT image without any correction, which is generated by reconstructing line integrals using the FDK algorithm. These line integrals are calculated through Eqn (4) using the flat field projection and all the measured CBCT projections acquired in one 360 degrees circular rotation. A quantitative evaluation of the proposed method's performance is executed by comparing the corrected images against the planning MDCT images, which are taken as ground truth. For these studies, the proposed method is performed on the CBCT images in axial, coronal, and sagittal views.

3.2 Method for statistical evaluation

The three factors used to evaluate the success of shading correction are discussed in this section.

3.2.1 Mean CT number, SNU values, and image contrast

Shading correction in images can be evaluated qualitatively by observing the images before and after the corrections. The performance of the proposed method can also be evaluated quantitatively by selecting ROIs and calculating the RMSE of CT

number, SNU value, and image contrast. These three evaluation parameters effectively measure the presence of the main CT image artifacts, which are scattering, non-uniformity, and blurring.

To obtain the CT numbers used for parameter calculations, four uniform ROIs are selected in each patient's pCT, uncorrected CT, Varian corrected CT, and proposed method CT. The ROIs are chosen in different areas of the same tissue type as shown in Figure 6. All values are taken in HU.

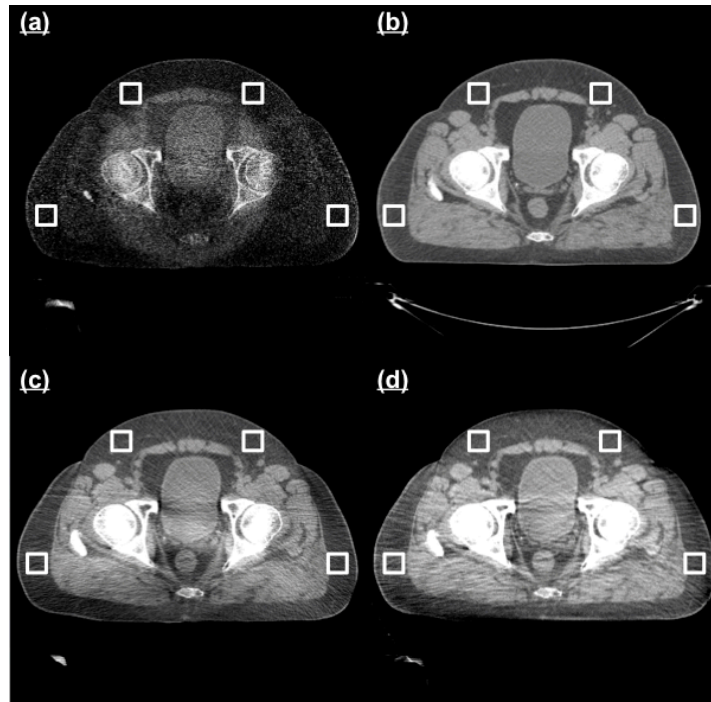


Figure 6: Four selected uniform soft-tissue ROIs in axial images
ROIs marked with solid white squares; the image quality is compared amongst (a) CBCT without correction, (b) pCT as ground truth, (c) Varian corrected CBCT, and (d) CBCT corrected by proposed method.

Between the two sets of shading corrected images (i.e. the CT images corrected by Varian algorithm and by the proposed algorithm), the better image after correction will more closely resemble the ground truth (i.e. pCT). To compare the similarities between the ground truth and the scatter corrected images, the CT number error is calculated as the square root of the mean square error (i.e. RMSE) as shown in Eqn (8),

$$RMSE = \sqrt{\frac{1}{N} \sum_{i=1}^N (x_i - x_i')^2} \quad \text{Eqn (8)}$$

where N is the total number of ROIs, i is the index of the ROI, x_i is the mean ROI value of CT images, and x_i' is the corresponding mean ROI value measured in the reference image.

SNU is described by Eqn (9). It reflects the non-uniformity of CT images, and is caused by low-frequency errors in the projection data. Image contrast of an image is illustrated by Eqn (11),

$$SNU = \frac{\overline{HU}_{max} - \overline{HU}_{min}}{1000} \times 100\% \quad \text{Eqn (9)}$$

where SNU is spatial non-uniformity value, \overline{HU}_{max} and \overline{HU}_{min} are the maximum and minimum mean CT numbers measured inside the ROIs for each patient respectively. Eqn

(10) illustrates how the SNU error between the ground truth and shading corrected images is determined.

$$SNU\ error = |SNU_{pCT} - SNU_{corrected\ CBCT}| \quad \text{Eqn (10)}$$

$$C = |x_i - x_b| \quad \text{Eqn (11)}$$

where C is the image contrast value, x_i and x_b are the mean CT value inside the ROI of the CT image and the mean CT value in the background respectively. The error of image contrast between the ground truth and shading corrected images is then calculated using Eqn (12). Statistical analysis is performed on the CBCT images in axial, coronal, and sagittal views.

$$C\ error = |C_{pCT} - C_{corrected\ CBCT}| \quad \text{Eqn (12)}$$

where $C\ error$ is the error of image contrast, C_{pCT} is the contrast value of the ground true, and $C_{corrected\ CBCT}$ is the contrast value of the shading corrected CBCT.

3.2.2 Paired t-test

A paired t-test is carried out to determine if the proposed method can consistently correct CBCT image scatter for many different patient data sets without bias. It is used to compare the error in CT number, SNU error, and image contrast error before and after the shading correction.

To determine if the quality of images corrected by Varian is worse than the quality of images corrected by the proposed method, hypotheses are set up to test if the errors from the three evaluation parameters are greater for the Varian corrected images than they are for the images corrected using the proposed method. As shown in Eqn (13), the null hypothesis (H_0) tests that the difference between the true mean errors of the two populations is zero, while the alternative hypothesis (H_1) tests that the true mean of the first population is greater than the true mean of the second population. [8],

$$\begin{aligned} H_0: \mu_1 - \mu_2 &= \delta = 0 \\ H_1: \mu_1 - \mu_2 &= \delta > 0 \end{aligned} \tag{Eqn (13)}$$

where H_0 is the null hypothesis, H_1 is the alternative hypothesis, μ_1 represents the mean value of a parameter in the first population, μ_2 represents the mean value of the parameter in the second population, and δ is the difference between the true mean values of the two population.

To perform the statistical analyses on the two populations of shading corrected images in terms of the three errors of image quality, let the first population consist of the images corrected by the Varian algorithm and let the second population the images corrected by the proposed method. Let the two populations with standard normal distributions have the sample sizes n_1 and n_2 respectively, the means μ_1 and μ_2 respectively, the known variances σ_1^2 and σ_2^2 respectively, and the degrees of freedom, ν_1

and v_2 respectively. Depending on the particular test being performed, the mean values and variances will represent either those of *RMSE*, *SNU error*, or *C error* within a population.

Since each set of images from the first population (i.e. Varian corrected images) and the second population (i.e. images corrected by the proposed method) are from the same patient, the parameters being tested are assumed to be normally distributed and have equal variances across populations. Under this assumption, Eqn (7) can be rewritten as Eqn (14).

$$t = \frac{\hat{u}_1 - \hat{u}_2 - \delta}{s_p \sqrt{\frac{1}{n_1} + \frac{1}{n_2}}} \quad \text{Eqn (14)}$$

where n_1 and n_2 are the sample sizes for first and second populations respectively, \hat{u}_1 and \hat{u}_2 are the sample mean values in the first and second populations respectively, and s_p is a factor that is derived from the Z distribution value, which is described in Eqn (7), when the variances are assumed to be equal.

$$s_p^2 = \frac{(n_1 - 1)s_1^2 + (n_2 - 1)s_2^2}{n_1 + n_2 - 2} \quad \text{Eqn (15)}$$

where s_1 and s_2 are the standard deviation of the samples from the first and second populations respectively. Since there are 20 set of patient data for both populations (i.e. $n_1 = n_2$), Eqn (15) can also be rewritten as Eqn (16).

$$s_p^2 = \frac{1}{2}(s_1^2 + s_2^2) \quad \text{Eqn (16)}$$

Since the sum of the two population sample sizes is 40, the degrees of freedom (ν) is calculated by Eqn (5) to be 38. The t value for a ν of 38 and the confidence level $(1 - \alpha)$ of 95% (i.e. $t_{0.05,38}$) is found in a t-distribution table and compared to the t-value calculated using Eqn (14). If the calculated t-value is greater than $t_{0.05,38}$, the null hypothesis stated in Eqn (13) is rejected. Hence, one can conclude that that μ_1 is greater than μ_2 with 95% confidence.

CHAPTER 4 - RESULTS

The proposed method of CBCT shading correction is evaluated on 20 sets of thorax and pelvis cancer patient data from CTCA in Newnan, Georgia. Since there are always 81 Varian corrected CBCT image slices in the patient data sets used for this thesis, the corrected CBCT images using the proposed method are reconstructed to 81 slices to complete a reliable comparison. Details about the 20 sets of patient data, which include the number of projections and element spacing, are listed in Table 8 of Appendix A. The measured CT numbers used to calculate the mean CT numbers across the four ROIs for each image in the axial, coronal, and sagittal views are listed Appendix A.

4.1 Qualitative results

The CBCT images with no correction, the corresponding pCT, the corrected CBCT by Varian method, and the corrected CBCT by the proposed method in axial, coronal, and sagittal views are compared side by side.

4.1.1 Axial view images

Comparing the CBCT axial images, 20 out of 20 shading corrected images have better image qualities than the images without any corrections. 17 out of 20 of the proposed method corrected images have better quality than the Varian corrected images. Axial images of patient A (Figure 7) and patient B (Figure 8) are shown as examples of

the CBCT images where the proposed method is successfully applied to enhance the quality of the Varian corrected image. The spatial non-uniformity in the center of the patient is less severe in the image corrected by the proposed method (Figure 7d). Axial images of patient H (Figure 9) and patient L (Figure 10) are shown as examples of challenging cases, where the CBCT image quality is comparable between the proposed correction method and the Varian correction method.

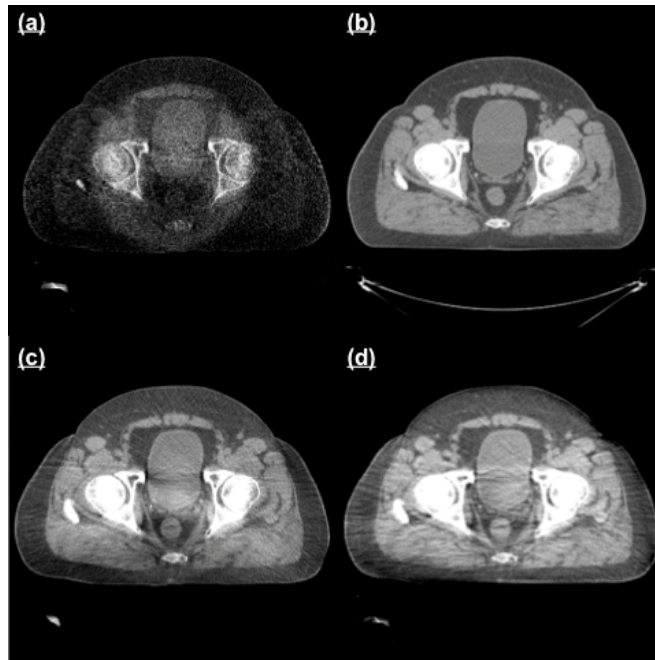


Figure 7: First example of successful shading corrected axial CBCT images (Patient A) amongst 20 sets of total sample size.
Successful shading correction as shown by (a) CBCT without correction, (b) pCT as ground truth, (c) Varian corrected CBCT, and (d) CBCT corrected by proposed method.

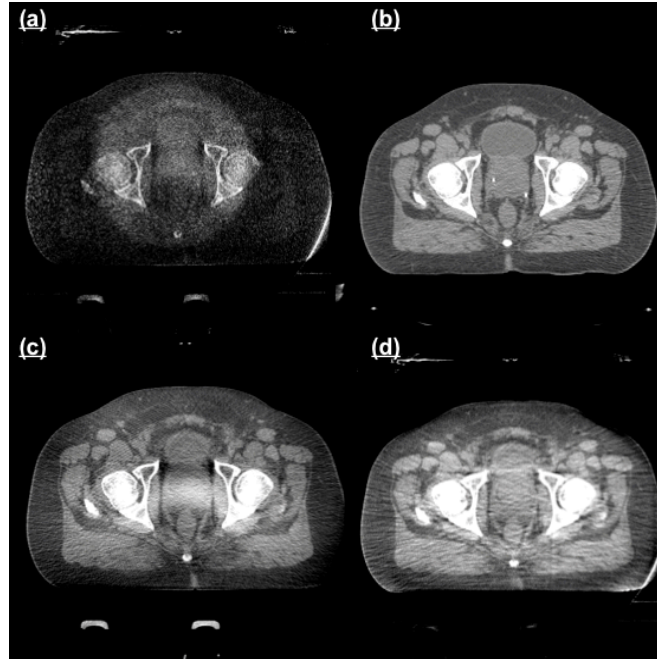


Figure 8: Second example of successful shading corrected axial CBCT images (Patient B) amongst 20 sets of total sample size.

Successful shading correction as shown by (a) CBCT without correction, (b) pCT as ground truth, (c) Varian corrected CBCT, and (d) CBCT corrected by proposed method.

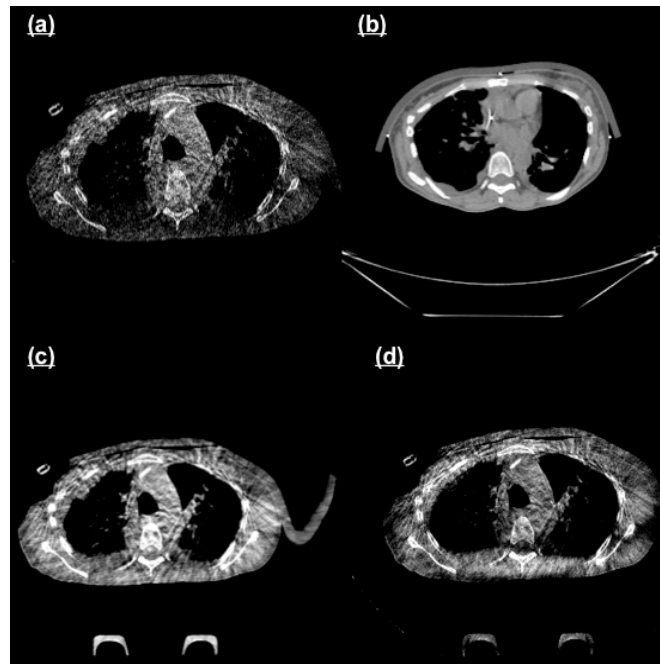


Figure 9: First example of challenging axial CBCT images (Patient H) for shading correction. Challenging but comparable results are shown by (a) CBCT without correction, (b) pCT as ground truth, (c) Varian corrected CBCT, and (d) CBCT corrected by proposed method.

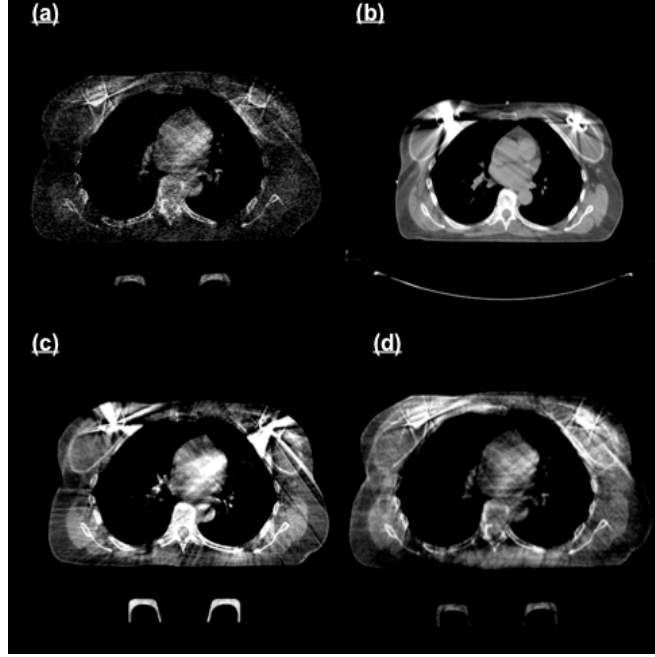


Figure 10: Second example of challenging axial CBCT images (Patient L) for shading correction. Challenging but comparable results are shown by (a) CBCT without correction, (b) pCT as ground truth, (c) Varian corrected CBCT, and (d) CBCT corrected by proposed method.

4.1.2 Coronal and sagittal view images

The CBCT images are also compared in coronal and sagittal views. Images with more bony anatomy structure (i.e. pelvis images) have better correction results than others (e.g. thorax images). Coronal and sagittal images of patient A (Figure 11) and patient B (Figure 12) are shown as examples of the coronal and sagittal CBCT images where the proposed method is successfully applied to enhance the quality of the Varian corrected image. Coronal and sagittal images of patient H (Figure 13) and patient L (Figure 14) are shown as examples of the CBCT images, where shading correction is more challenging. The coronal and sagittal images of patients H and L that corrected by the proposed method are comparable to the images of the Varian corrected images.

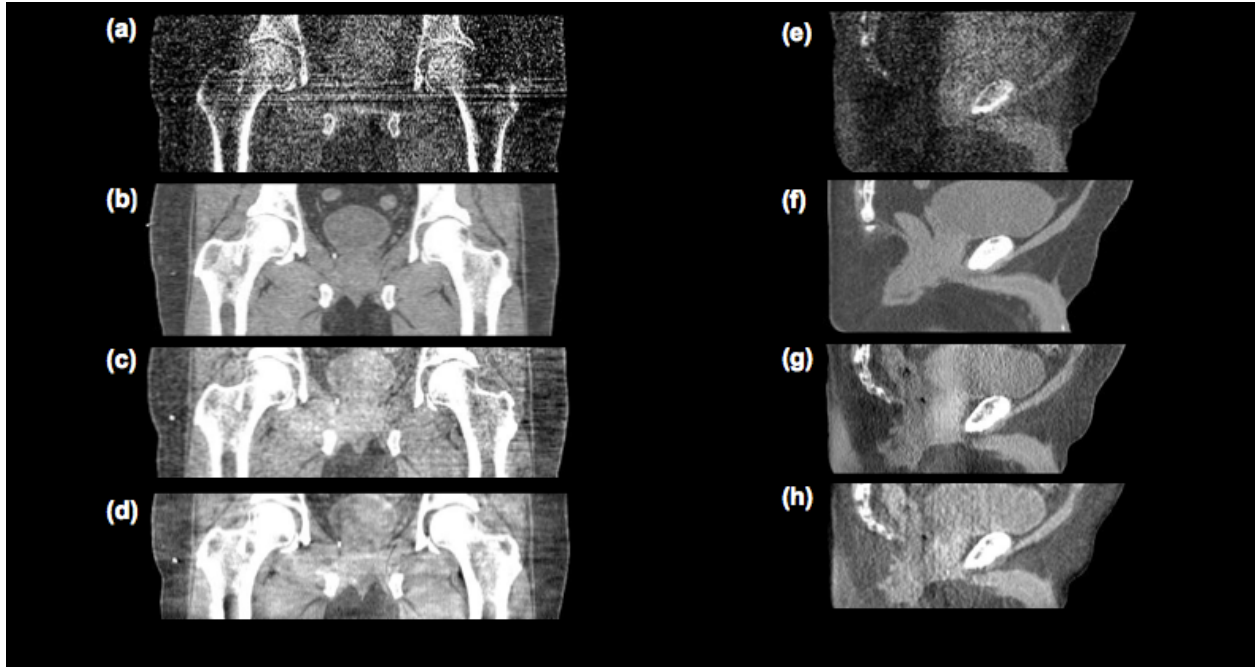


Figure 11: First example of successful shading corrected CBCT images (Patient A) in coronal and sagittal views.

Successful shading correction as shown by (a) coronal CBCT without correction, (b) coronal pCT as ground truth, (c) Varian corrected coronal CBCT, (d) coronal CBCT corrected by proposed method, (e) sagittal CBCT without correction, (f) sagittal pCT as ground truth, (g) Varian corrected sagittal CBCT, and (h) sagittal CBCT corrected by proposed method.

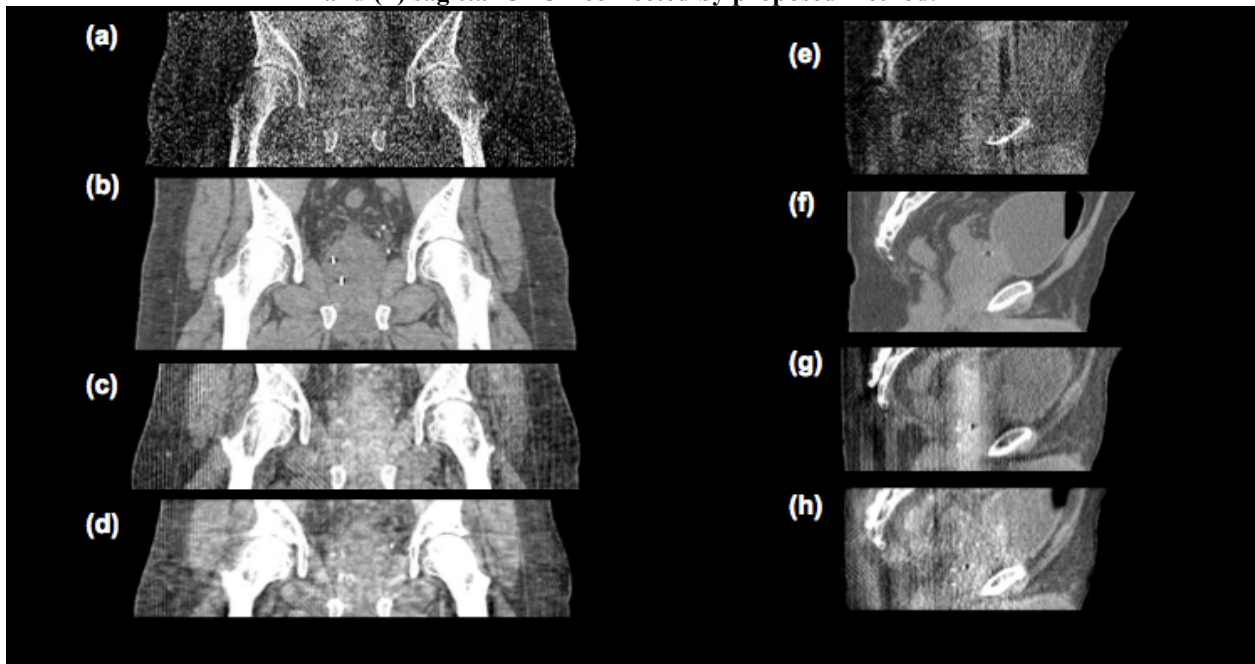


Figure 12: Second example of successful shading corrected CBCT images (Patient B) in coronal and sagittal views.

Successful shading correction as shown by (a) coronal CBCT without correction, (b) coronal pCT as ground truth, (c) Varian corrected coronal CBCT, (d) coronal CBCT corrected by proposed method, (e) sagittal CBCT without correction, (f) sagittal pCT as ground truth, (g) Varian corrected sagittal CBCT, and (h) sagittal CBCT corrected by proposed method.

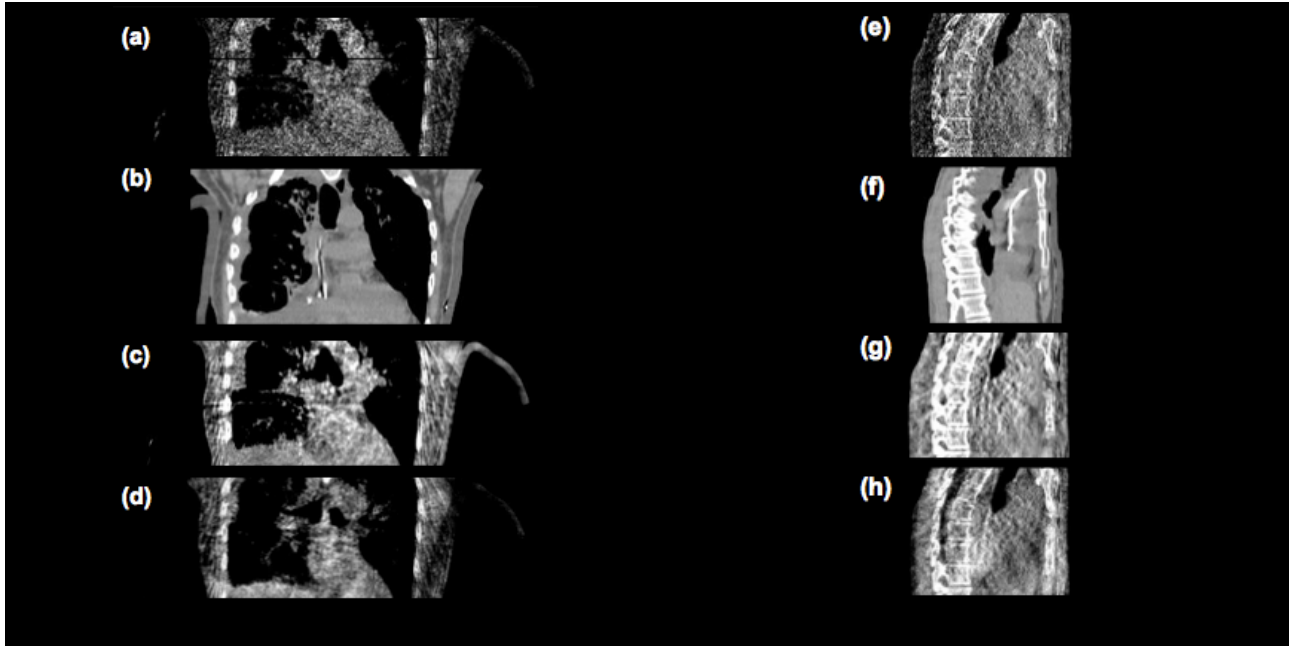


Figure 13: First example of challenging images (patient H) in coronal and sagittal views for shading correction.

Challenging but comparable results are shown by (a) coronal CBCT without correction, (b) coronal pCT as ground truth, (c) Varian corrected coronal CBCT, (d) coronal CBCT corrected by proposed method, (e) sagittal CBCT without correction, (f) sagittal pCT as ground truth, (g) Varian corrected sagittal CBCT, and (h) sagittal CBCT corrected by proposed method.

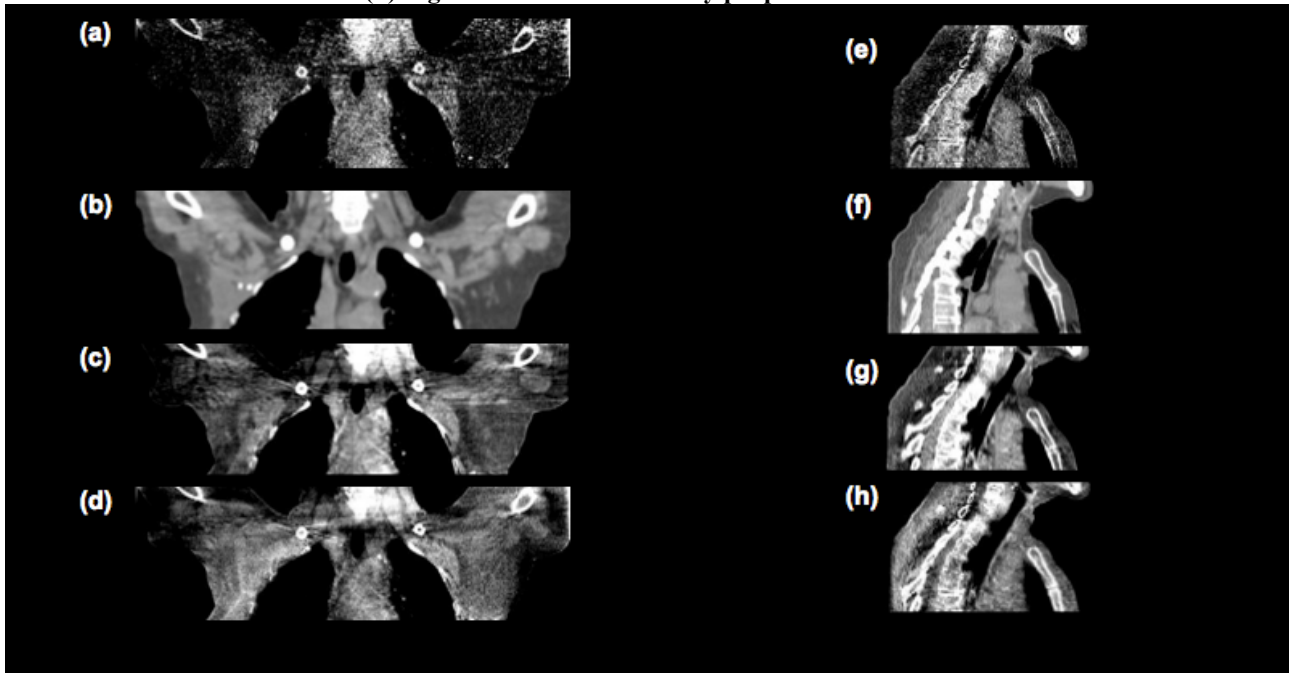


Figure 14: Second example of challenging images (patient L) in coronal and sagittal views for shading correction.

Challenging but comparable results are shown by (a) coronal CBCT without correction, (b) coronal pCT as ground truth, (c) Varian corrected coronal CBCT, (d) coronal CBCT corrected by proposed method, (e) sagittal CBCT without correction, (f) sagittal pCT as ground truth, (g) Varian corrected sagittal CBCT, and (h) sagittal CBCT corrected by proposed method.

4.2 Quantitative results

Quantitative evaluation of the proposed algorithm on images with axial views is shown by the computation of mean CT number errors (i.e. RMSE), SNU errors, and image contrast errors, which are presented in section 4.2.1. Similarly, the RMSE, SNU errors, and image contrast errors for coronal view images are presented in section 4.2.2, and the errors for sagittal view images are presented in section 4.2.3.

The average of RMSE, SNU errors, and contrast errors amongst axial, coronal, and sagittal view in CBCT images corrected by the Varian method and the proposed method are calculated and summarized following Table 1. On average, the errors in CT numbers, SNU, and contrast values are greater in Varian corrected CBCT images. This indicates that the images corrected by the proposed method generally have better image quality. Further discussion on the consistency and reliability of this generalized statement will be made later in this paper.

Table 1: Summary of average errors in CBCT corrected by Varian and proposed methods.

	Average RMSE	Average SNU error	Average contrast error
Varian corrected CBCT image	52.682 HU	7.293 %	36.805 HU
Proposed method corrected CBCT image	40.523 HU	2.966 %	34.077 HU
Difference	12.159 HU	4.327 %	2.728 HU

4.2.1 Axial view images

The average RMSE, SNU errors, and contrast errors for the uncorrected images, Varian corrected CBCT, and CBCT corrected by the proposed method in the axial view are summarized in Table 2. The raw values for all 20 patient data sets are displayed in Appendix B.

Table 2: Average errors in CT numbers, SNU, and contrast values for images in axial view

Axial view			
	Average RMSE	Average SNU error	Average contrast error
Between ground truth and no correction images	141.813 HU	9.822 %	140.342 HU
Between ground truth and Varian corrected images (first population)	60.111 HU	7.078 %	40.906 HU
Between ground truth and proposed method corrected images (second population)	39.125 HU	2.935 %	35.571 HU

When performing the paired t-test to evaluate the difference between the errors of the first and second populations (i.e. Varian corrected images and images corrected by the proposed method, respectively), the errors of the two populations are assumed to be normally distributed and have equal variances since the two corresponding populations are from the same patients. To determine if the errors in the Varian corrected images are higher than the errors the images corrected by the proposed method, the null hypothesis (H_0) of $\mu_1 - \mu_2 = 0$ and the alternative hypothesis (H_1) of $\mu_1 - \mu_2 > 0$ are tested at the 95% level of confidence for the errors of CT numbers, SNU, and image contrast.

To compare the errors in CT numbers of the CBCT images using the two correction methods, the average RMSE must first be determined for each sample. Using Eqn (8), the 20 sets from the first population are found to have an average RMSE of 60 HU with a standard deviation of 48 HU, while those from the second population are found to have an average RMSE of 39 HU with a standard deviation of 30 HU. Using the paired t-test, the null hypothesis is rejected as t is found to be 1.669, which exceeds the $t_{0.05,38}$ of 1.645. Therefore, with 95% confidence, one can conclude that on average CT numbers of the first population contain more error than those of the second.

Secondly, in the comparison of the SNU errors, calculations using Eqn (10) find that the 20 samples from the first population have an average SNU error of 7.08%, while the 20 samples from the second population have an average SNU error of 2.94%. The null hypothesis is again rejected as t is found to be 1.928, which exceeds the $t_{0.05,38}$ of 1.645. Therefore, with 95% confidence, one can conclude that images from the first population generally have larger SNU errors than do images from the second.

Lastly, in the comparison of the errors in image contrast, calculations using Eqn (12) find that the 20 samples from the first population have an average contrast error of 41 HU, while the 20 samples from the second population have an average contrast error of 36 HU with a standard deviation of 4 HU. The null hypothesis is accepted as t is found to be 0.700, which is smaller than the $t_{0.05,38}$ of 1.645. Therefore, there is neither

significant image contrast improvement nor degradation between the first and second populations.

The summary of the paired t-test results for the three evaluation parameters are shown in Table 3.

Table 3: Values for paired t-test calculations for axial view

Axial view			
	RMSE	SNU error	Image contrast error
ν	38		
\hat{u}_1	60.111 HU	7.078 %	40.907 HU
\hat{u}_2	39.125 HU	2.935 %	35.571 HU
s_1	47.860 HU	9.266 %	41.184 HU
s_2	29.532 HU	2.556 %	33.454 HU
s_p	39.766	6.797	24.087
t	1.669	1.928	0.700
$t_{0.05,38}$	1.645		
Reject H_0?	Yes, Reject with 95% confidence	Yes, Reject with 95% confidence	No

4.2.2 Coronal view images

The RMSE, SNU errors, and contrast errors for the uncorrected images, Varian corrected CBCT, and CBCT corrected by the proposed method in the coronal view are shown in Table 4. The raw values for all 20 patient data sets are displayed in Appendix B.

Table 4: Average errors in CT numbers, SNU, and contrast values for images in coronal view

Coronal view			
	Average RMSE	Average SNU error	Average contrast error
Between ground truth and no correction images	130.123 HU	9.817 %	131.702 HU
Between ground truth and Varian corrected images (first population)	45.715 HU	6.890 %	32.736 HU
Between ground truth and proposed method corrected images (second population)	38.792 HU	2.970%	32.705 HU

With the same assumption and hypotheses as the axial images, the errors between the two correction methods in coronal views are evaluated using paired t-test. Table 5 summarizes the results of the three paired t-test for coronal images. The calculated t-values for the difference in RMSE and contrast error are both too small to reject the null hypothesis at the 95% confidence level. However, as shown in Table 5, there is a statistically significant improvement at the 95% confidence level with respect to SNU error.

Table 5: Values for paired t-test calculations for coronal view

Coronal view			
	RMSE	SNU error	Image contrast error
ν	38		
\hat{u}_1	45.715 HU	6.890 %	32.736 HU
\hat{u}_2	38.792 HU	2.970 %	32.705 HU
s_1	30.160 HU	5.303 %	26.744 HU
s_2	22.915 HU	2.547 %	25.644 HU
s_p	16.662	2.428	18.498
t	1.314	5.106	0.005
$t_{0.05,38}$	1.645		
Reject H_0?	No	Yes, Reject with 95% confidence	No

4.2.3 Sagittal view images

The RMSE, SNU errors, and contrast errors for the uncorrected images, Varian corrected CBCT, and CBCT corrected by the proposed method in the sagittal view are shown in Table 6. The raw values for all 20 patient data sets are displayed in Appendix B.

Table 6: Average errors in CT numbers, SNU, and contrast values for images in sagittal view

Sagittal view			
	Average RMSE	Average SNU error	Average contrast error
Between ground truth and no correction images	117.442 HU	7.174 %	159.793 HU
Between ground truth and Varian corrected images (first population)	52.219 HU	7.911 %	36.772 HU
Between ground truth and proposed method corrected images (second population)	43.653 HU	2.994 %	33.955 HU

With the same assumption and hypotheses as the axial and coronal images, the errors between the two correction methods in sagittal views are evaluated using paired t-test. Table 7 summarizes the results of the three paired t-test for sagittal images. The calculated t-values for the difference in RMSE and contrast error are both too small to reject the null hypothesis at the 95% confidence level. However, as shown in Table 7, there is a statistically significant improvement at the 95% confidence level with respect to SNU error.

Table 7: Values for paired t-test calculations for sagittal view

Sagittal view			
	RMSE	SNU error	Image contrast error
ν	38		
\hat{u}_1	52.219 HU	7.911%	36.772 HU
\hat{u}_2	43.653 HU	2.994%	33.955 HU
s_1	26.706 HU	4.736%	30.709 HU
s_2	39.715 HU	2.547%	28.042 HU
s_p	28.319	2.369	20.21
t	1.032	6.564	0.441
$t_{0.05,38}$	1.645		
Reject H_0 ?	No	Yes, Reject with 95% confidence	No

CHAPTER 5 - DISCUSSION

As demonstrated in Figure 7(d) and Figure 8(d), those images successfully corrected by the proposed method exhibit an overall reduction in scattering artifacts and central non-uniformity. This improvement could help physicians better identify soft tissues or abnormalities in the center and periphery of patients' CBCT images. The summary in Table 1 and the qualitative observations in section 4.2.1 suggest that on average the proposed method can successfully enhance CBCT image quality and overcome the weaknesses in Varian corrected images. Furthermore, in all of the quantitative studies (9 in total) the proposed method reduced the error in the CBCT images on average. Conducted t-tests show that half of these improvements are statistically significant at the 95% confidence level.

The errors of CT numbers and SNU indicate the severity of scattering and non-uniformity artifacts. As shown in Table 2, the error of CT number errors fell from 60 HU in Varian corrected axial images to 39 HU in axial images corrected by the proposed method. Similarly, the errors of SNU fell from 7.08% in Varian corrected axial images to 2.94% in the axial images corrected by the proposed method, from 6.89% to 2.97% in the coronal images, and from 7.91% to 2.99% in the sagittal images. These improvements with respect to CT numbers and SNU achieved by using the proposed method are concluded to be statistically significant at the 95% confidence level.

Similar to axial images, the errors of CT numbers in coronal and sagittal images are reduced from 46 HU to 39 HU and 52 HU to 44 HU respectively. However, the differences in RMSE for the two sample sets do not allow us to reject the null hypothesis of $\mu_1 - \mu_2 = 0$ with 95% confidence. Therefore, there is not a statistically significant improvement in RMSE between the first and second populations. Hence, the results suggest that the proposed method is more successful with respect to RMSE for axial images than it is for coronal and sagittal images. This may be caused by the limitations of the image dimensions, where shading corrections are more apparent in larger axial images (512 by 512) versus corrections in small coronal and sagittal images (512 by 81).

The image contrast errors in the 20 sets of patient data are also calculated for the images produced using the two different shading correction methods. The average contrast error is reduced from 41 HU in the Varian corrected axial images to 36 HU in the axial images corrected by the proposed method, and from 37 HU to 34 HU in sagittal images. However, the slight improvement in error is statistically insignificant at the 95% confidence level and hence the null hypothesis of $\mu_1 - \mu_2 = 0$ cannot be rejected. The average contrast errors between the Varian corrected coronal images and the coronal images corrected by the proposed method remain the same as 33 HU, thus the null hypothesis again cannot be rejected. The statistically small reduction of image contrast errors suggests that the proposed method does not improve nor degrade the image contrast of the CBCT images.

Notice that the outlines of the pCT (image b) are very well defined comparing to the other three images, and the delineation of the outline is lost when the three images (images a, c, and d) are reconstructed from the projections. The blurring and distortion on the outline is normally difficult to overcome due to the limitations of the FDK reconstruction algorithm. However, the outline of the CBCT image corrected using the proposed method is comparable to that of the Varian corrected image, as shown in the case of patient A (Figure 7) and the outline of the CBCT image corrected using the proposed method is better and easier to define than that of the Varian corrected CBCT in the case of patient B (Figure 8).

The proposed method successfully corrected 17 out of 20 sets of patient data in the axial view, most of which are pelvis images. Pelvis images are easier to correct because there is more bony anatomy present, which expedites image registration results. The other three image sets were more challenging for both the Varian and proposed methods due to severe motion artifacts. Using patient H (Figure 9) and patient L (Figure 10) as two examples, these images are all thorax images and with large motion artifacts. Since the respiratory motions are not monitored nor gated when these CT images are taken, there are drastic geometrical differences between pCT and CBCT images, which leads to unsuccessful image registration results. Figure 15 is an image with overlay, which shows the mismatch between the primary image (displayed in green) and the registration result (displayed in purple). An additional factor that contributed to shading correction failure for patient H is the addition of tubes for medicinal purposes. The image registration quality is poor since the tube position cannot be held constant between the

pCT and CBCT images. Furthermore, the tube is very close to the body of patient H and cannot be easily segmented out by manually adjusting the ROI in the Velocity image registration software. Specific reasons that cause challenges in shading correction for patient L include the symmetrical implants of high contrast materials in both sides of the breasts. The high contrast materials cause severe scattering and cannot be segmented out because they are inside the patient.

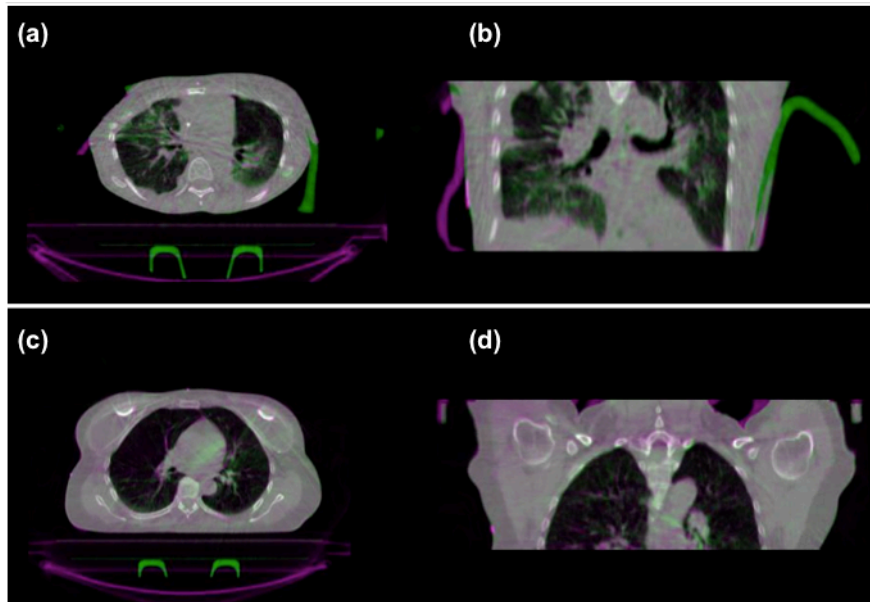


Figure 15: Unsuccessful image registration for thorax images.
Demonstrating the differences between the fixed image (displayed in green) and the registered MDCT result (displayed in purple); with image (a) shows the axial slice of patient H, (b) shows the coronal slice of patient H, (c) shows the axial slice of patient L, and (d) shows the coronal slice of patient L.

CHAPTER 6 - CONCLUSION

In conclusion, the proposed method of shading correction using MDCT as prior knowledge improves the quality of CBCT images produced through the current industry standard, the Varian algorithm. This improvement by the proposed method further enhances the appearance of structural and tissue details in the CBCT images produced by the Varian algorithm. The Varian corrected images have more severe scattering and non-uniformity artifacts compared to the proposed method corrected images, which is shown by the calculated errors in CT number and SNU. The contrast error of images corrected by the proposed method also shows a slight but statistically insignificant improvement over that of the Varian corrected images. The shading in CBCT images with larger motion artifacts (e.g. respiratory motions) is more challenging to correct than the shading in CBCT images containing more high contrast bony structures. However, as an extension of a previously developed and similar method for shading correction, which was evaluated through phantom studies [1], the results presented in this thesis confirms the efficacy of the proposed correction method using patient studies. Thus, this work shows that the CBCT image quality using current industrial correction algorithm, e.g. Varian algorithm, can be significantly improved by employing planning MDCT as a prior knowledge as performed using the proposed method of CBCT shading correction.

APPENDIX A - RAW DATA

Table 8: Image details of the 20 sets of patient data

Patient Data Set	Description	Number of raw CBCT Projections	Number of Varian corrected CBCT slices	Element spacing of Varian corrected CBCT (mm)	Number of MDCT slices	Element spacing of pCT (mm)
A	Pelvis	656	81	0.908203 0.908203 1.98988	303	1.26953 1.26953 1.25
B	Pelvis	656	81	0.908203 0.908203 1.98988	233	1.26953 1.26953 1.25
C	Pelvis	656	81	0.908203 0.908203 1.98988	233	1.26953 1.26953 1.25
D	Pelvis	656	81	0.908203 0.908203 1.98988	286	0.976562 0.976562 1.25
E	Pelvis	656	81	0.908203 0.908203 1.98988	286	0.976562 0.976562 1.25
F	Pelvis, pediatric	656	81	0.908203 0.908203 1.98988	193	0.994141 0.994141 2.5
G	Pelvis	656	81	0.908203 0.908203 1.98988	354	1.26953 1.26953 1.25
H	Thorax	656	81	0.908203 0.908203 1.98988	174	1.26953 1.26953 2.5
I	Pelvis	655	81	0.908203 0.908203 1.98988	228	1.26953 1.26953 2.5
J	Pelvis	655	81	0.908203 0.908203 1.98988	181	1.26953 1.26953 2.5
K	Thorax	655	81	0.908203 0.908203 1.98988	178	1.26953 1.26953 2.5
L	Thorax	656	81	0.908203 0.908203 1.98766	152	1.26953 1.26953 2.5

Table 8: (continued)

M	Thorax	656	81	0.908203 0.908203 1.98988	159	1.26953 1.26953 2.5
N	Pelvis	656	81	0.908203 0.908203 1.98766	272	1.26953 1.26953 2.5
O	Thorax	656	81	0.908203 0.908203 1.98988	154	1.26953 1.26953 2.5
P	Thorax	656	81	0.908203 0.90820 1.98988	182	1.26953 1.26953 2.5
Q	Thorax	656	81	0.908203 0.908203 1.98988	164	1.26953 1.26953 2.5
R	Pelvis	656	81	0.908203 0.908203 1.98988	322	1.26953 1.26953 1.25
S	Thorax	655	81	0.908203 0.908203 1.98988	163	1.26953 1.26953 2.5
T	Thorax	654	81	0.908203 0.908203 1.98988	121	1.26953 1.26953 2.5

**Table 9: Raw and mean CT values of axial images for 20 patient data sets.
Showing the four selected ROI CT numbers (HU) of pCT, no correction CT, Varian corrected CT,
and proposed method corrected CT.**

Axial view					
Patient	ROI	pCT mean CT	No Correction mean CT	Varian mean CT	Corrected mean CT
A	1	-108.95	-205.24	-97.69	-64.70
	2	-100.56	-223.89	-118.21	-81.23
	3	-91.28	-222.55	-129.95	-92.11
	4	-100.15	-284.98	-115.69	-87.35
	mean A	-100.24	-234.16	-115.38	-81.35
B	1	-107.39	-155.94	-101.51	-99.67
	2	-97.75	-207.38	-115.33	-78.71
	3	-98.65	-243.82	-140.33	-96.25
	4	-95.88	-268.30	-152.46	-117.63
	mean B	-99.92	-218.86	-127.41	-98.06
C	1	-103.31	-145.04	-84.12	-88.52
	2	-98.73	-224.25	-115.08	-86.34
	3	-97.95	-225.67	-192.81	-113.34
	4	-99.07	-288.30	-170.63	-100.58
	mean C	-99.77	-220.82	-140.66	-97.19
D	1	-111.12	-249.99	-96.90	-82.29
	2	-83.16	-247.47	-137.69	-78.66
	3	-90.60	-245.45	-128.40	-101.21
	4	-95.19	-220.06	-134.93	-78.94
	mean D	-95.02	-240.74	-124.48	-85.27
E	1	-110.03	-237.11	-87.02	-112.32
	2	-86.28	-361.95	-87.02	-80.25
	3	-86.28	-268.42	-132.76	-79.80
	4	-87.35	-268.42	-126.59	-103.49
	mean E	-92.49	-283.98	-108.35	-93.97
F	1	-214.70	-110.83	-91.91	-83.43
	2	-233.20	-94.00	-92.94	-93.57
	3	-203.29	-98.44	-98.99	-123.27
	4	-218.87	-117.64	-53.98	-123.91
	mean F	-217.51	-105.23	-84.46	-106.04

Table 9: (continued)

G	1	-105.84	-187.93	-100.15	-73.88
	2	-100.46	-189.06	-110.33	-57.20
	3	-102.51	-229.70	-68.91	-83.16
	4	-101.83	-229.70	-97.75	-43.03
	mean G	-102.66	-209.10	-94.28	-64.32
H	1	34.56	-5.08	51.40	-14.41
	2	40.10	-88.23	54.37	-12.77
	3	34.51	-94.64	-75.21	-39.01
	4	47.97	-148.92	19.86	-37.69
	mean H	39.28	-84.22	12.60	-25.97
I	1	-110.39	-81.63	-6.48	-71.17
	2	-106.91	-181.35	-18.55	-105.67
	3	-112.42	-247.13	35.66	-61.32
	4	-99.07	-141.46	-36.19	-73.40
	mean I	-107.20	-162.89	-6.39	-77.89
J	1	-109.63	-218.10	-67.13	-92.09
	2	-106.43	-203.27	-74.46	-113.53
	3	-108.51	-231.49	-88.32	-108.82
	4	-94.63	-272.10	-98.44	-122.20
	mean J	-104.80	-231.24	-82.09	-109.16
K	1	-108.82	-196.02	-75.99	-105.25
	2	-88.78	-213.61	-62.99	-99.46
	3	-94.83	-215.69	-64.68	-104.80
	4	-90.67	-270.56	-83.52	-136.14
	mean K	-95.78	-223.97	-71.79	-111.41
L	1	-97.04	-217.99	-218.00	-190.80
	2	-111.64	-231.97	-130.39	-171.18
	3	-109.83	-266.86	-69.21	-234.69
	4	-104.69	-281.98	-131.74	-194.41
	mean L	-105.80	-249.70	-137.33	-197.77
M	1	-93.43	-154.13	-148.37	-85.13
	2	-78.21	-240.80	-102.51	-107.14
	3	-72.33	-363.83	-2.65	-10.67
	4	-90.79	-244.39	-95.03	-135.52
	mean M	-83.69	-250.79	-87.14	-84.61
N	1	-105.44	-135.79	-122.47	-91.75
	2	-103.22	-279.61	-159.76	-80.21
	3	-109.04	-265.34	-107.35	-73.70
	4	-93.04	-148.07	-172.31	-93.48
	mean N	-102.68	-207.20	-140.47	-84.78

Table 9: (continued)

O	1	-110.67	-369.57	-524.86	29.68
	2	-75.49	-150.26	-222.55	-58.18
	3	-105.40	-132.05	-66.23	-12.26
	4	-77.32	-289.91	-159.10	-92.37
	mean O	-92.22	-235.45	-243.18	-33.28
P	1	-107.70	-220.63	-140.95	-111.56
	2	-109.91	-203.41	-119.89	-52.82
	3	-89.83	-214.28	-118.09	-98.05
	4	-124.82	-389.78	-203.00	-124.29
	mean P	-108.06	-257.02	-145.48	-96.68
Q	1	-97.94	-272.14	-119.19	-77.76
	2	-82.94	-150.78	-82.95	-80.21
	3	-89.45	-279.05	-195.75	-82.57
	4	-100.12	-216.13	-165.22	-83.20
	mean Q	-92.61	-229.53	-140.78	-80.94
R	1	-111.03	-226.10	-101.13	-62.86
	2	-97.53	-280.95	-173.40	-87.06
	3	-94.73	-199.55	-121.33	-86.83
	4	-111.49	-268.96	-144.53	-89.17
	mean R	-103.70	-243.89	-135.10	-81.48
S	1	-108.63	-171.32	-79.11	-50.54
	2	-102.94	-158.35	-95.77	-145.21
	3	-95.33	-248.01	-135.91	-141.06
	4	-89.85	-276.71	-125.43	-148.11
	mean S	-99.19	-213.60	-109.06	-121.23
T	1	-99.96	-101.10	-103.85	-81.36
	2	-72.30	-263.59	-173.04	-73.95
	3	-57.00	-307.77	-88.10	-74.11
	4	-25.52	-222.34	-120.05	-104.31
	mean T	-63.70	-223.70	-121.26	-83.43

Table 10: Raw and mean CT values of coronal images for 20 patient data sets.
Showing the four selected ROI CT numbers (HU) of pCT, no corrected CT, Varian corrected CT, and proposed method corrected CT.

Coronal view					
Patient	ROI	pCT mean CT	No Correction mean CT	Varian mean CT	Corrected mean CT
A	1	-108.85	-210.40	-91.78	-78.39
	2	-102.17	-223.46	-98.01	-84.35
	3	-116.93	-213.23	-120.10	-82.21
	4	-110.00	-216.89	-113.38	-96.94
	mean A	-109.49	-215.99	-105.82	-85.47
B	1	-92.03	-197.81	-154.58	-89.30
	2	-100.21	-199.29	-107.17	-64.09
	3	-84.88	-204.94	-66.18	-91.67
	4	-99.51	-206.69	-85.57	-83.56
	mean B	-94.16	-202.18	-103.37	-82.16
C	1	-92.17	-234.99	-142.86	-68.00
	2	-103.05	-204.49	-106.22	-97.03
	3	-91.51	-223.19	-182.08	-100.45
	4	-102.61	-164.37	-141.59	-132.15
	mean C	-97.33	-206.76	-143.18	-99.41
D	1	-90.33	-228.99	-129.07	-132.02
	2	-94.35	-217.87	-67.58	-103.89
	3	-85.20	-241.87	-129.30	-140.97
	4	-76.42	-194.39	-106.13	-108.25
	mean D	-86.58	-220.78	-108.02	-121.28
E	1	-90.55	-233.00	-111.41	-88.84
	2	-99.00	-215.15	-71.98	-72.67
	3	-79.23	-222.98	-114.21	-78.34
	4	-99.51	-205.07	-109.59	-81.62
	mean E	-92.07	-219.05	-101.80	-80.37
F	1	-89.23	-187.17	-68.46	-91.65
	2	-105.78	-234.80	-91.69	-90.39
	3	-115.96	-211.94	-77.53	-94.85
	4	-119.75	-255.81	-107.10	-93.27
	mean F	-107.68	-222.43	-86.19	-92.54

Table 10: (continued)

G	1	-95.78	-190.10	-69.05	-76.24
	2	-95.37	-238.88	-107.80	-70.48
	3	-104.64	-226.42	-102.22	-69.10
	4	-82.03	-192.38	-115.20	-47.53
	mean G	-94.45	-211.94	-98.57	-65.84
H	1	-48.45	-173.54	-52.15	0.89
	2	-63.60	-150.01	7.50	-32.55
	3	-55.30	-23.62	-2.47	-64.90
	4	-44.31	-118.93	-29.83	-22.40
	mean H	-52.92	-116.52	-19.24	-29.74
I	1	-104.46	-215.68	-201.65	-121.45
	2	-109.17	-137.27	-177.45	-104.17
	3	-107.36	-304.80	-171.29	-62.44
	4	-106.64	-336.23	-242.14	-50.97
	mean I	-106.91	-248.50	-198.13	-84.76
J	1	-107.09	-247.19	-77.81	-114.26
	2	-108.97	-205.40	-51.95	-113.88
	3	-109.00	-282.44	-142.81	-89.65
	4	-115.35	-211.80	-65.06	-55.36
	mean J	-110.10	-236.71	-84.41	-93.29
K	1	-101.93	-228.70	-126.93	-46.83
	2	-106.08	-291.98	-14.33	26.98
	3	-115.08	-275.32	-98.12	-14.71
	4	-104.89	-210.58	-201.43	-61.50
	mean K	-107.00	-251.65	-110.20	-24.01
L	1	-121.53	-338.17	-151.67	-95.58
	2	-115.80	-203.50	-221.36	-115.89
	3	-118.00	-404.95	-85.19	-84.23
	4	-126.87	-375.17	-105.80	-78.32
	mean L	-120.55	-330.45	-141.00	-93.51
M	1	-107.45	-251.18	-134.28	-171.83
	2	-111.07	-248.54	-270.68	-160.80
	3	-116.29	166.26	-183.14	-167.69
	4	-108.07	-174.24	-126.03	-165.95
	mean M	-110.72	-126.92	-178.53	-166.57

Table 10: (continued)

N	1	-113.77	-205.19	-103.80	-84.95
	2	-112.23	-66.93	-146.37	-120.03
	3	-109.20	22.52	-120.30	-72.06
	4	-112.43	-151.72	-86.22	-90.63
	mean N	-111.91	-100.33	-114.17	-91.92
O	1	-117.80	-220.45	-234.77	-119.08
	2	-127.11	-160.65	-243.41	-17.36
	3	-106.75	-389.75	-291.09	-31.84
	4	-109.33	-380.99	-69.00	-127.88
	mean O	-115.25	-287.96	-209.57	-74.04
P	1	-116.85	-204.10	-82.83	-59.70
	2	-112.00	-264.11	-134.24	-49.85
	3	-107.11	-249.63	-159.92	-48.94
	4	-110.86	-245.36	-117.88	-53.23
	mean P	-111.70	-240.80	-123.72	-52.93
Q	1	-105.23	-162.82	-115.53	-110.26
	2	-109.00	-205.19	-118.99	-47.90
	3	-118.82	-268.65	-170.47	-137.69
	4	-107.90	-211.45	-180.71	-78.93
	mean Q	-110.24	-212.03	-146.43	-93.69
R	1	-110.07	-225.32	-136.36	-102.31
	2	-130.67	-196.81	-146.69	-115.01
	3	-116.29	-190.16	-113.60	-101.02
	4	-104.10	-156.24	-133.39	-102.34
	mean R	-115.28	-192.13	-132.51	-105.17
S	1	-118.70	-260.59	-115.64	-36.07
	2	-84.19	-163.83	-162.18	-5.29
	3	-111.52	-275.30	-75.00	24.06
	4	-98.93	-225.96	-168.14	-48.36
	mean S	-103.34	-231.42	-130.24	-16.42
T	1	-109.46	-191.09	-106.48	-83.06
	2	-101.72	-134.40	-91.12	-96.35
	3	-79.81	-202.66	-71.64	-83.87
	4	-76.63	-237.62	-72.31	-55.61
	mean T	-91.90	-191.44	-85.39	-79.72

**Table 11: Raw and mean CT values of sagittal images for 20 patient data sets.
Showing the four selected ROI CT numbers (HU) of pCT, no correction CT, Varian corrected CT,
and proposed method corrected CT.**

Sagittal view					
Patient	ROI	pCT mean CT	No Correction mean CT	Varian mean CT	Corrected mean CT
A	1	-105.44	-243.74	-117.06	-108.90
	2	-114.39	-231.61	-70.01	-116.56
	3	-110.98	-201.45	-112.14	-118.76
	4	-95.44	-190.07	-156.92	-108.04
	mean A	-106.56	-216.71	-114.03	-113.07
B	1	-108.57	-214.09	-82.33	-96.48
	2	-103.98	-158.21	-50.56	-119.85
	3	-105.17	-132.44	-169.32	-81.56
	4	-108.38	-130.18	-190.65	-115.91
	mean B	-106.52	-158.73	-123.22	-103.45
C	1	-105.18	-212.94	-99.90	-92.30
	2	-108.35	-167.99	-59.96	-111.01
	3	-102.25	-139.25	-173.92	-125.50
	4	-103.93	-303.78	-144.97	-112.37
	mean C	-104.93	-205.99	-119.69	-110.29
D	1	-112.92	-251.92	-106.95	-138.75
	2	-105.58	-234.81	-72.60	-120.13
	3	-108.66	-273.03	-56.19	-140.79
	4	-108.49	-131.21	-140.64	-126.43
	mean D	-108.91	-222.74	-94.10	-131.52
E	1	-107.45	-238.73	-110.08	-95.54
	2	-112.40	-239.29	-86.38	-95.05
	3	-113.25	-223.84	-5.57	-90.32
	4	-110.06	-106.68	-68.45	-107.35
	mean E	-110.79	-202.13	-67.62	-97.06
F	1	-103.71	-267.40	-53.46	-131.76
	2	-107.46	-254.82	-57.76	-140.26
	3	-105.39	-213.15	69.07	-148.10
	4	-106.14	-271.52	30.15	-194.24
	mean F	-105.68	-251.72	-3.00	-153.59

Table 11: (continued)

G	1	-98.58	-157.58	-102.79	-92.04
	2	-98.83	-195.23	-96.23	-91.95
	3	-99.68	-131.84	-85.17	-82.87
	4	-93.24	-126.23	-91.72	-91.10
	mean G	-97.58	-152.72	-93.98	-89.49
H	1	54.92	-219.16	-54.59	-9.11
	2	51.88	-163.05	46.93	-4.89
	3	45.00	-272.56	72.90	14.43
	4	39.83	-28.73	39.80	-6.75
	mean H	47.91	-170.87	26.26	-1.58
I	1	-107.10	-241.06	-233.28	-82.47
	2	-113.52	-256.89	-141.52	-91.52
	3	-97.15	-263.05	-175.18	-69.72
	4	-101.96	-288.03	-133.67	-52.11
	mean I	-104.93	-262.26	-170.91	-73.95
J	1	-93.86	-260.91	-136.16	-108.78
	2	-92.93	-270.87	-99.91	-80.49
	3	-106.92	-238.78	-69.81	-77.74
	4	-106.67	-194.28	15.31	-76.50
	mean J	-100.09	-241.21	-72.64	-85.88
K	1	-116.57	-204.58	-71.53	-24.88
	2	-106.13	-156.46	-62.03	-37.85
	3	-110.97	-137.06	-83.53	-60.24
	4	-107.25	-209.07	-42.73	-12.43
	mean K	-110.23	-176.79	-64.95	-33.85
L	1	-113.13	-243.57	-114.87	79.06
	2	-107.15	-246.82	-95.88	88.66
	3	-97.67	-232.02	-95.99	78.00
	4	-97.17	-266.08	-103.23	24.40
	mean L	-103.78	-247.12	-102.49	67.53
M	1	-116.14	-146.98	0.39	-30.29
	2	-116.20	-194.43	-148.27	-53.96
	3	-118.53	-153.17	-157.17	6.09
	4	-108.56	-155.09	-168.89	-43.14
	mean M	-114.86	-162.42	-118.48	-30.33
N	1	-104.31	-164.47	-122.67	-94.55
	2	-106.27	-129.68	-108.33	-82.79
	3	-108.33	-137.99	-177.76	-75.62
	4	-113.14	-126.86	-211.06	-86.45
	mean N	-108.01	-139.75	-154.96	-84.85

Table 11: (continued)

O	1	-103.17	-288.61	-225.64	-92.58
	2	-91.60	-324.60	-176.30	-113.61
	3	-107.75	-366.43	-202.14	-91.39
	4	-134.03	-332.61	-159.02	-93.98
	mean O	-109.14	-328.06	-190.78	-97.89
P	1	-116.74	-260.79	-138.31	-4.65
	2	-110.67	-279.59	-164.86	-87.30
	3	-107.92	-296.20	-126.97	-24.89
	4	-96.79	-293.72	-126.62	-71.44
	mean P	-108.03	-282.57	-139.19	-47.07
Q	1	-87.44	-232.11	-120.01	-87.19
	2	-78.85	-218.67	-142.00	-121.27
	3	-96.09	-171.57	-108.71	-31.60
	4	-108.00	-253.15	-203.52	3.12
	mean Q	-92.60	-218.88	-143.56	-59.24
R	1	-107.20	-158.34	-119.06	-108.47
	2	-105.23	-126.58	-88.23	-87.16
	3	-108.14	-136.02	-130.16	-88.76
	4	-100.88	-154.64	-118.60	-85.26
	mean R	-105.36	-143.90	-114.01	-92.41
S	1	-111.33	-208.44	-230.57	-127.99
	2	-123.57	-297.28	-119.39	-118.96
	3	-113.47	-384.31	-127.96	-72.21
	4	-118.85	-206.51	-85.17	-44.29
	mean S	-116.80	-274.13	-140.77	-90.86
T	1	-107.33	-65.14	-108.39	-169.59
	2	-98.83	-71.36	-113.79	-123.63
	3	-89.50	-71.27	-39.74	-116.92
	4	-99.67	-108.15	-64.42	-120.40
	mean T	-98.83	-78.98	-81.59	-132.64

APPENDIX B – ERRORS IN CT NUMBERS, SNU, AND CONTRAST VALUES FOR ALL PATIENT DATA

**Table 12: RMSE values of axial images
For 20 sets of patient data**

Axial view			
Patient data set	RMSE between ground truth and no correction images	RMSE between ground truth and Varian corrected images (first population)	RMSE between ground truth and proposed method corrected images (second population)
A	137.727	23.319	24.983
B	127.652	36.341	15.008
C	131.924	60.734	12.364
D	146.507	39.318	17.518
E	198.812	32.519	9.274
F	113.366	134.922	114.181
G	108.529	17.857	41.003
H	135.542	57.700	66.965
I	81.106	105.455	34.675
J	130.160	28.505	16.721
K	132.434	25.997	23.946
L	145.946	65.887	94.839
M	186.202	46.049	40.956
N	121.956	49.429	22.168
O	172.136	224.387	84.999
P	163.698	45.047	28.906
Q	145.223	63.225	13.674
R	143.760	43.744	27.343
S	127.697	30.966	51.592
T	185.885	70.826	41.377
Overall average	141.813	60.111	39.125

**Table 13: SNU values and errors of axial images
For 20 sets of patient data**

Axial view							
Patient data set	SNU value (pCT)	SNU value (No correction CBCT)	SNU value (Varian corrected CBCT)	SNU value (Proposed method corrected CBCT)	SNU error (No correction CBCT)	SNU error (Varian corrected CBCT)	SNU error (Proposed method corrected CBCT)
A	1.767	7.974	3.226	2.741	6.207	1.459	0.974
B	1.152	11.235	5.095	3.892	10.084	3.944	2.740
C	0.536	14.325	10.869	2.700	13.789	10.333	2.163
D	2.796	2.993	4.079	2.255	0.197	1.283	0.541
E	2.375	12.484	4.574	3.251	10.110	2.200	0.877
F	2.990	2.364	4.500	4.048	0.627	1.510	1.058
G	0.538	4.177	4.142	4.013	3.639	3.604	3.474
H	1.346	14.384	12.958	2.624	13.038	11.612	1.279
I	1.335	16.550	7.184	4.435	15.215	5.850	3.100
J	1.500	6.883	3.131	3.012	5.384	1.632	1.512
K	2.004	7.454	2.053	0.580	5.450	0.049	1.424
L	1.460	6.399	14.879	6.351	4.939	13.419	4.891
M	2.110	20.970	14.572	9.647	18.860	12.462	7.538
N	1.600	14.382	6.495	1.977	12.782	4.896	0.377
O	3.517	23.753	45.862	12.205	20.235	42.345	8.688
P	3.499	18.637	8.491	7.147	15.138	4.991	3.648
Q	1.718	12.827	11.280	0.544	11.109	9.562	1.174
R	1.676	8.140	7.228	2.631	6.464	5.552	0.955
S	1.878	11.836	5.680	9.757	9.958	3.802	7.879
T	7.444	20.667	8.494	3.035	13.223	1.050	4.409
Overall average	2.162	11.922	9.240	4.342	9.822	7.078	2.935

**Table 14: Image contrast values and errors of axial images
For 20 sets of patient data**

Axial view							
Patient data set	Contrast (pCT)	Contrast (No correction CBCT)	Contrast (Varian corrected CBCT)	Contrast (Proposed method corrected CBCT)	Contrast error (No correction CBCT)	Contrast error (Varian corrected CBCT)	Contrast error (Proposed method corrected CBCT)
A	897.053	742.751	884.464	815.523	154.302	12.588	81.530
B	885.738	873.687	872.253	856.378	12.051	13.485	29.359
C	898.329	691.646	858.844	832.896	206.683	39.485	65.433
D	882.425	699.413	875.227	868.220	183.012	7.198	14.206
E	870.816	674.371	891.538	854.467	196.445	20.722	16.348
F	763.376	899.681	915.545	890.149	136.305	152.169	126.773
G	873.618	769.611	904.948	931.615	104.007	31.330	57.997
H	1035.380	910.333	1012.605	972.682	125.047	22.776	62.698
I	891.920	787.809	993.042	879.565	104.112	101.122	12.355
J	872.618	942.053	917.899	875.737	69.435	45.281	3.119
K	899.018	791.772	927.378	880.558	107.245	28.360	18.459
L	881.585	722.021	862.252	799.612	159.564	19.333	81.973
M	906.213	740.612	912.714	905.879	165.601	6.500	0.334
N	888.915	768.672	859.392	916.687	120.243	29.524	27.772
O	891.871	647.009	756.514	926.586	244.862	135.357	34.716
P	886.022	724.017	849.663	897.040	162.006	36.360	11.018
Q	898.803	751.211	858.621	911.897	147.593	40.183	13.093
R	890.645	751.876	862.861	925.540	138.770	27.784	34.895
S	889.850	778.995	890.912	875.269	110.855	1.062	14.581
T	926.158	767.461	878.646	921.390	158.697	47.512	4.768
Overall average	891.518	771.750	889.266	886.885	140.342	40.906	35.571

**Table 15: RMSE values of coronal images
For 20 sets of patient data**

Coronal view			
Patient data set	RMSE between ground truth and no correction images	RMSE between ground truth and Varian corrected images (first population)	RMSE between ground truth and proposed method corrected images (second population)
A	106.913	9.089	25.599
B	108.290	33.559	20.077
C	113.846	55.454	19.826
D	135.040	35.513	38.575
E	128.051	24.949	15.945
F	116.148	23.806	18.637
G	118.849	22.221	29.390
H	86.146	44.916	31.507
I	161.905	95.597	36.849
J	130.682	44.103	31.818
K	147.885	68.287	90.416
L	222.834	58.249	32.288
M	175.899	88.016	56.148
N	85.596	22.773	26.202
O	203.444	125.312	67.087
P	131.487	33.503	58.805
Q	106.937	45.208	35.192
R	80.365	21.288	11.634
S	131.751	55.264	92.184
T	110.386	7.186	37.660
Overall average	130.123	45.715	38.792

**Table 16: SNU values and errors of coronal images
For 20 sets of patient data**

Coronal view							
Patient data set	SNU value (pCT)	SNU value (No correction CBCT)	SNU value (Varian corrected CBCT)	SNU value (Proposed method corrected CBCT)	SNU error (No correction CBCT)	SNU error (Varian corrected CBCT)	SNU error (Proposed method corrected CBCT)
A	0.783	1.306	2.832	1.855	0.523	2.049	1.071
B	1.533	0.888	8.840	2.757	0.645	7.308	1.225
C	1.154	7.062	7.585	6.414	5.909	6.432	5.261
D	1.793	4.748	6.172	3.708	2.955	4.379	1.914
E	2.028	2.793	4.223	1.617	0.765	2.195	0.411
F	3.052	6.864	10.710	0.446	3.812	7.658	2.606
G	2.262	4.878	4.615	0.714	2.617	2.353	1.547
H	1.929	14.991	5.965	6.579	13.063	4.036	4.650
I	0.472	19.895	7.085	5.902	19.424	6.614	5.430
J	0.827	7.703	7.774	5.890	6.877	6.948	5.064
K	1.315	8.140	18.711	4.678	6.825	17.396	3.363
L	1.107	20.145	13.617	3.756	19.038	12.511	2.650
M	0.883	41.743	14.464	1.103	40.860	13.581	0.220
N	0.456	22.771	6.015	4.797	22.315	5.558	4.341
O	2.036	22.910	22.209	11.052	20.874	20.172	9.016
P	0.974	6.001	7.708	1.077	5.027	6.734	0.103
Q	1.359	10.583	6.518	8.979	9.224	5.159	7.620
R	2.657	3.516	3.309	1.399	0.859	0.652	1.257
S	3.451	11.147	9.314	4.307	7.696	5.863	0.856
T	3.284	10.322	3.484	4.074	7.038	0.200	0.791
Overall average	1.668	11.420	8.558	4.055	9.817	6.890	2.970

**Table 17: Image contrast values and errors of coronal images
For 20 sets of patient data**

Coronal view							
Patient data set	Contrast (pCT)	Contrast (No correction CBCT)	Contrast (Varian corrected CBCT)	Contrast (Proposed method corrected CBCT)	Contrast error (No correction CBCT)	Contrast error (Varian corrected CBCT)	Contrast error (Proposed method corrected CBCT)
A	863.076	733.230	885.394	854.411	129.847	22.318	8.666
B	881.203	739.254	886.180	869.729	141.949	4.977	11.474
C	880.275	755.705	855.976	853.744	124.570	24.299	26.530
D	881.654	726.473	889.567	776.092	155.181	7.913	105.562
E	871.165	724.833	896.704	898.157	146.332	25.539	26.992
F	837.581	770.340	899.143	864.854	67.241	61.562	27.273
G	875.311	763.883	895.924	934.259	111.428	20.613	58.948
H	945.304	873.457	978.689	897.669	71.847	33.385	47.634
I	887.857	700.419	801.868	923.604	187.438	85.989	35.747
J	869.098	740.940	915.399	911.774	128.158	46.301	42.677
K	883.735	735.789	888.920	897.736	147.946	5.185	14.001
L	872.219	630.598	857.699	833.082	241.622	14.520	39.138
M	884.550	851.586	812.822	821.761	32.964	71.728	62.789
N	831.762	818.078	881.461	860.729	13.684	49.699	28.967
O	881.740	486.483	790.297	817.939	395.257	91.443	63.801
P	876.029	774.613	871.375	881.500	101.416	4.654	5.470
Q	878.834	771.680	852.038	891.641	107.155	26.796	12.807
R	833.314	784.493	863.896	859.561	48.822	30.581	26.246
S	885.505	749.631	866.080	878.506	135.873	19.425	6.999
T	901.227	755.905	909.023	903.599	145.322	7.796	2.372
Overall average	876.072	744.369	874.923	871.517	131.702	32.736	32.705

**Table 18: RMSE values of sagittal images
For 20 sets of patient data**

Sagittal view			
Patient data set	RMSE between ground truth and no correction images	RMSE between ground truth and Varian corrected images (first population)	RMSE between ground truth and proposed method corrected images (second population)
A	111.809	38.357	7.682
B	61.836	60.052	15.906
C	118.828	47.933	14.006
D	126.049	35.038	23.625
E	106.746	59.184	15.618
F	147.879	116.194	53.497
G	61.023	7.702	9.711
H	238.146	56.557	51.056
I	158.624	77.137	32.898
J	145.462	67.254	23.123
K	73.019	47.143	78.477
L	144.140	6.514	173.863
M	51.078	70.251	88.108
N	36.178	60.727	24.643
O	220.812	89.034	24.837
P	175.725	34.113	71.846
Q	129.657	59.856	67.647
R	41.047	17.527	15.391
S	173.670	62.409	43.474
T	27.110	31.397	37.660
Overall average	117.442	52.219	43.653

**Table 19: SNU values and errors of sagittal images
For 20 sets of patient data**

Sagittal view							
Patient data set	SNU value (pCT)	SNU value (No correction CBCT)	SNU value (Varian corrected CBCT)	SNU value (Proposed method corrected CBCT)	SNU error (No correction CBCT)	SNU error (Varian corrected CBCT)	SNU error (Proposed method corrected CBCT)
A	1.000	5.367	8.691	1.072	4.368	7.691	0.072
B	0.459	8.391	14.009	3.829	7.932	13.549	3.370
C	0.610	16.454	11.396	3.320	15.844	10.786	2.710
D	0.734	14.182	8.445	2.066	13.448	7.711	1.332
E	0.580	13.261	10.452	1.702	12.680	9.871	1.122
F	0.376	5.837	12.683	6.248	5.462	12.307	5.872
G	0.643	6.899	1.762	0.916	6.256	1.119	0.273
H	1.508	24.383	12.749	0.422	22.875	11.240	1.086
I	1.637	4.697	9.961	3.941	3.060	8.324	2.304
J	1.399	7.659	15.146	2.828	6.260	13.747	1.429
K	1.043	7.201	4.080	1.245	6.158	3.037	0.202
L	1.596	2.251	1.900	6.426	0.655	0.304	4.830
M	0.997	4.744	16.928	6.005	3.747	15.931	5.008
N	0.883	3.762	10.273	1.893	2.879	9.390	1.010
O	4.243	7.782	6.662	2.103	3.539	2.420	2.140
P	1.996	3.541	3.824	8.265	1.545	1.828	6.270
Q	2.915	8.158	9.480	12.439	5.243	6.565	9.524
R	0.727	3.177	4.193	2.321	2.450	3.467	1.594
S	1.223	17.780	14.540	7.467	16.556	13.317	6.244
T	1.783	4.302	7.405	5.267	2.518	5.622	3.484
Overall average	1.318	8.491	9.229	3.989	7.174	7.911	2.994

**Table 20: Image contrast values and errors of sagittal images
For 20 sets of patient data**

Sagittal view							
Patient data set	Contrast (pCT)	Contrast (No correction CBCT)	Contrast (Varian corrected CBCT)	Contrast (Proposed method corrected CBCT)	Contrast error (No correction CBCT)	Contrast error (Varian corrected CBCT)	Contrast error (Proposed method corrected CBCT)
A	884.364	736.761	880.293	886.604	147.603	4.071	2.239
B	888.205	768.173	807.283	890.109	120.032	80.922	1.905
C	891.736	664.130	853.715	859.272	227.605	38.021	32.464
D	882.499	703.150	895.991	819.657	179.349	13.492	62.843
E	868.298	698.311	863.078	814.444	169.987	5.220	53.854
F	883.332	742.398	987.097	846.543	140.934	103.765	36.788
G	898.787	710.471	902.590	911.550	188.316	3.803	12.763
H	1046.70 1	820.747	987.833	944.116	225.953	58.867	102.584
I	876.976	688.856	826.658	925.683	188.120	50.318	48.707
J	895.840	723.390	925.341	896.388	172.450	29.502	0.548
K	886.402	714.589	924.785	972.703	171.813	38.383	86.301
L	894.331	719.260	897.505	916.231	175.071	3.173	21.900
M	883.207	827.484	881.516	889.610	55.723	1.690	6.403
N	878.307	838.688	845.042	903.924	39.619	33.265	25.617
O	883.174	695.440	809.207	864.954	187.735	73.968	18.220
P	881.916	688.490	859.387	942.313	193.426	22.529	60.397
Q	902.097	735.889	846.949	920.166	166.208	55.148	18.069
R	890.401	822.700	880.258	920.165	67.702	10.143	29.763
S	839.116	572.388	757.903	800.470	266.727	81.212	38.646
T	890.421	778.938	918.361	871.338	111.483	27.940	19.083
Overall average	892.305	732.513	877.540	889.812	159.793	36.772	33.955

REFERENCES

1. Niu, T., et al., *Shading correction for on-board cone-beam CT in radiation therapy using planning MDCT images*. Med Phys, 2010. **37**(10): p. 5395-406.
2. Niu, T., A. Al-Basheer, and L. Zhu, *Quantitative cone-beam CT imaging in radiation therapy using planning CT as a prior: first patient studies*. Med Phys, 2012. **39**(4): p. 1991-2000.
3. Scarfe, W.C. and A.G. Farman *What is Cone-beam CT and How Does it Work?* The Dental Clinics of North America, 2008.
4. Bushberg, J.T., et al., *Computed Tomography*, in *The Essential Physics of Medical Imaging*. 2011, Lippincott Williams & Wilkins.
5. Miller, I. and M. Miller, *Sampling Distribution*, in *John E. Freund's Mathematical Statistics with Application*. 2004, Person Prentice Hall: New Jersey. p. 0-13-124646-1.
6. Star-Lack, J., et al., *Efficient Scatter Correction Using Asymmetric Kernels*. Physics of Medical Imaging, 2009. **7258**.
7. Zhu, L., J. Wang, and L. Xing, *Noise suppression in scatter correction for cone-beam CT*. Med Phys, 2009. **36**(3): p. 741-52.
8. Miller, I. and M. Miller, *Tests of Hypothesis Involving Means, Variances, and Proportions*, in *John E. Freund's Mathematical Statistics with Application*. 2004, Person Prentice Hall: New Jersey.